Probing Reactive Platinum Sites in UiO-67 Zirconium Metal−Organic Frameworks

Sigurd Øien,[†] Giovanni Agostini,[‡,§] Stian Svelle,[†] Elisa Borfecchia,[‡] Kirill A. Lomachenko,[‡,‖] Lorenzo Mino,[‡] Erik Gallo,[‡,§] Silvia Bordiga,[‡] Unni Olsbye,[†] Karl Petter Lillerud,*[,†] and Carlo Lamberti*[,‖,⊥]

[†]inGAP Centre for Research Based Innovation, Department of Chemistry, University of Oslo, P.O. Box 1033, N-0315 Oslo, Norway
[‡]Department of Chemistry, NIS and INSTM Reference Centers, University of Torino, Via Quarello 15, I-10135 Torino, Torino, Italy
[§]European Synchrotron Radiation Facility (ESRF), 6 Rue Jules Horowitz, BP 220, Grenoble, Cedex 9 38043, France
[‖]Southern Federal University, Zorge Street 5, 344090 Rostov-on-Don, Russia
[⊥]Department of Chemistry, CrisDi Centre for Crystallography, University of Torino, Via Giuria 7, I-10125 Torino, Torino, Italy

Ⓢ *Supporting Information*

ABSTRACT: We present three methods of the synthesis of zirconium metal−organic framework UiO-67 functionalized with platinum bipyridine coordination complexes (bpydcPt^{II}Cl$_2$ and bpydcPt^{IV}Cl$_4$) acting as linkers in the MOF framework. These Pt complexes can be reduced to bpydcPt^0 under flow of H$_2$ gas in the 600−700 K range, as probed by a sophisticated parametric refinement of in situ EXAFS data. IR spectroscopy testifies the high coordinative unsaturation of the reduced centers, able to form bpydcPt^0(CO)$_2$ dicarbonyl complexes upon CO adsorption. The large pore size of UiO-67 allows for ligand exchange between 2 Cl$^-$ and even bulky ligands such as toluene-3,4-dithiol. Framework bpydcPt^{II}Cl$_2$ complexes can also be oxidized at room temperature to bpydcPt^{IV}Br$_4$ through oxidative addition of liquid Br$_2$. XANES spectroscopy was used to monitor the changes in the Pt oxidation state along the observed reactions. Platinum bipyridine-functionalized UiO-67-Pt displays the same exceptional stability as the parent material as testified on both long and local range by in situ XRPD and Pt L$_3$-edge EXAFS data.
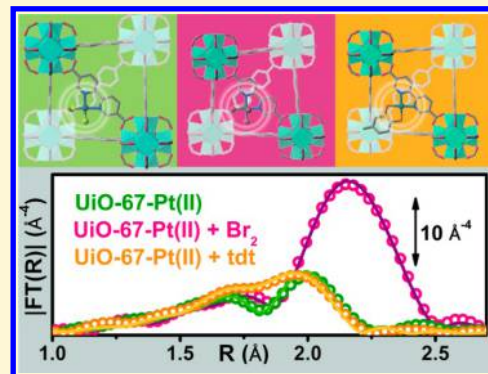
1. INTRODUCTION

Metal−organic frameworks (MOFs) are crystalline, porous solids consisting of discrete inorganic and organic secondary building units (SBUs),[1] which are currently gaining attention due to their properties as catalysts[2−7] and selective adsorbents.[8−13] One of the useful features of MOFs is the ability to incorporate sophisticated chemical functionalities[14−20] as part of the framework itself, thus making it possible to adapt homogeneous-phase catalysts into the solid state. Zirconium based MOFs are well suited to this adaption due to their stability toward water and high temperatures, and Zr biphenyl dicarboxylate MOF UiO-67, with a BET surface area of up to 2500 m^2/g and a pore size that can accommodate large chemical moieties, is of particular interest.[21,22]

Due to their structural similarity, biphenyl and bipyridine SBUs can occur in the same UiO-67 crystal in any ratio, thus opening the possibility to utilize the chelating ability of bipyridine as a backbone ligand for catalytically active metal complexes. There are numerous examples of this principle being utilized successfully in UiO-67.[23,24] Figure 1a reports the structure of the functionalized PtCl$_2$(H$_2$bpydc) linker. Part (b) reports the expected structure of UiO-67 MOF realized with a fraction of functionalized PtCl$_2$(H$_2$bpydc) linkers.

Introducing a chemically active Pt site as part of the UiO-67 framework is of great interest as a potential catalyst, as platinum has rich redox chemistry, showing 0, II, and IV stable oxidation states. Moreover, certain coordination complexes are known to be active in C−H bond activation.[25−29] In particular, the dichlorobipyrimidyl platinum(II), PtCl$_2$(bpym), performs the catalytic oxidation in fuming or concentrated sulfuric acid, achieving high yields of methanol with selectivity higher than 90%.[30,31] It is consequently of potential interest to investigate the possibility to heterogenize such process anchoring the active Pt(II) complex on some high surface area material such as recently shown by the group of Schüth, for polymers first[32,33] and for N-doped carbons[34] successively.

In this work, three main strategies were used to synthesize UiO-67-Pt(II/IV): a one-pot synthesis method (OPS), in which the Pt precursor is added directly to the MOF synthesis, a premade linker synthesis (PMLS) in which PtCl$_2$(H$_2$bpydc) or PtCl$_4$(H$_2$bpydc) are used as a SBU in the MOF synthesis, and a postsynthesis functionalization (PSF) where a platinum
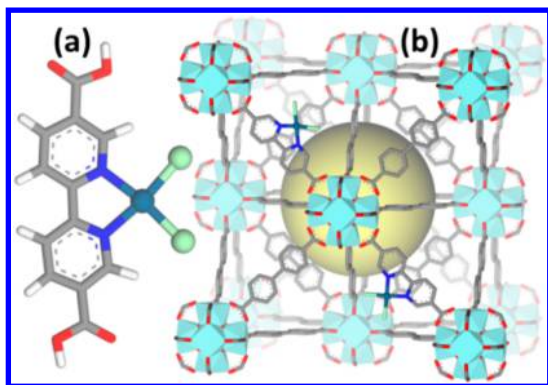
**Figure 1.** Part (a): structure of the isolated $H_2bpydcPtCl_2$ center inserted in the MOF structure showing 2 N and 2 Cl in the first coordination shell of Pt(II) and showing the distortion induced on the two rings by Pt insertion. Part (b) three-dimensional representation of Pt(II)-functionalized UiO-67 MOF.

chloride solution is reacted with UiO-67 with open bpy sites (see Figure 2). We used extended X-ray spectroscopy fine
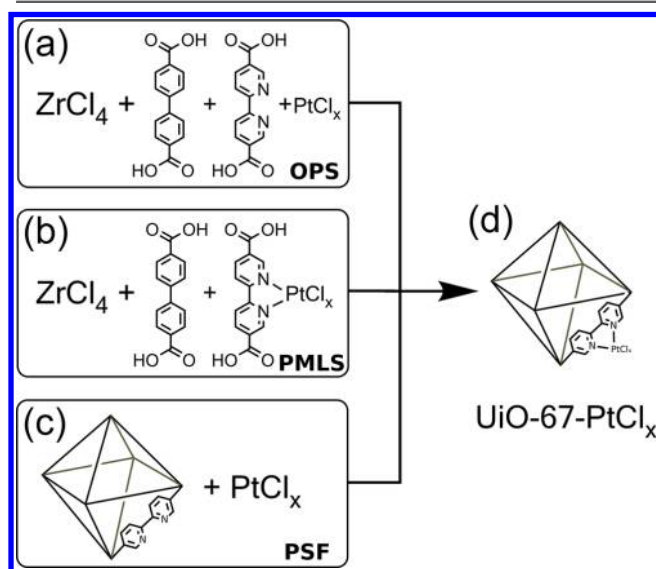
Figure 2. Scheme of the three different synthesis procedures adopted to obtain the final product UiO-67-bpy-PtCl$_x$ (x = 2 or 4), part (d). Part (a): mixing in one-pot $ZrCl_4$ and $PtCl_x$ precursor salts react with biphenyl and bipyridine linkers (OPS). Part (b): mixing biphenyl and $PtCl_x(H_2bpydc)$ (x = 2 or 4) prefunctionalized bipyridine linkers (PMLS). Part (c): reacting premade UiO-67-bpy MOF with precursor $PtCl_x$ salt (PSF).

structure (EXAFS) and valence-to-core resonant inelastic X-ray scattering (RIXS) techniques to prove the insertion of Pt atoms in the expected framework position of UiO-67, see Figure 1b.

Using EXAFS and XANES, the structural and oxidation state of Pt can be monitored under *in situ* conditions.[35−38] Elimination of chloride ligands from Pt in a continuous gas flow of H_2 have been monitored by EXAFS during temperature ramping. EXAFS also provided evidence of the liquid phase ligand exchange with toluene-3,4-dithiol and of the liquid phase oxidative addition of Br_2 to Pt. All observed reactions take place without any degradation of the framework.

2. EXPERIMENTAL AND METHODS

2.1. Sample Synthesis. *2.1.1. Synthesis of UiO-67 and Strategies for the Pt Insertion in the Lattice.* Pt-functionalized UiO-67 materials, hereafter UiO-67-Pt(II) and UiO-67-Pt(IV), were synthesized by the standard solvothermal method, by reacting $ZrCl_4$ with a mixture of H_2bpdc and $(H_2bpydc)/PtCl_x(H_2bpydc)$ (x = 2 or 4; the ratio between the linkers being 9:1, and equal molar quantity of $ZrCl_4$ and linker) in a solution of DMF. Five molar equivalents of benzoic acid were added to obtain a modulator effect, which resulted in a porous MOF with monodispersed particles and well-defined crystallinity.[39] Attempts of making UiO-67-Pt(II/IV) without using benzoic acid resulted in poorly crystalline, less porous material.

Pt insertion in the UiO-67 framework was achieved following using three different approaches: (i) $ZrCl_4$ and $PtCl_x$ (x = 2 or 4) precursor salts react with biphenyl and bipyridine linkers, named one-pot synthesis or OPS, see Figure 2a; (ii) previously prepared $PtCl_x(H_2bpydc)$ linker reacts with biphenyl linkers and $ZrCl_4$, named premade linker synthesis or PMLS, see Figure 2b; (iii) premade UiO-67-bpy MOF is suspended in a solution of precursor $PtCl_x$ salt, named postsynthesis functionalization or PSF, see Figure 2c. Assuming the platinum chloride will selectively coordinate to bipyridine, whereas zirconium will bind to the carboxylate groups, all methods should yield the same product.

The synthesis of H_2bpydc, $PtCl_2(H_2bpydc)$, and $PtCl_4(H_2bpydc)$ linkers is described in detail in the SI, together with their solid state ^{1}H NMR and single crystal XRD investigation.

2.1.2. Reactivity of Pt with Toluene-3,4-Dithiol and Br$_2$. In order to check the reactivity of square planar Pt(II) species inserted in the UiO-67 framework and the diffusion ability of large molecules, a fraction of UiO-67-Pt(II)_PSF sample was suspended in solutions of toluene-3,4-dithiol (H_2tdt) in 2-propanol at room temperature for 4 h. Although the reaction of toluene-3,4-dithiol (H_2tdt) with the $PtCl_2(H_2bpydc)$ linker is very fast, it takes some hours to react on UiO-67-Pt(II)_PSF MOF because of diffusion limitations. The so-obtained material will be labeled as UiO-67-Pt(II)_PSF_tdt. Analogously, a different fraction of UiO-67-Pt(II)_PSF sample was suspended in solutions of Br_2 in 2-propanol or in octane for 30 min at room temperature. The so-obtained materials will be labeled as UiO-67-Pt(II)_PSF_Br_p and UiO-67-Pt(II)_PSF_Br_o, respectively.

2.2. Laboratory Characterization. *2.2.1. X-ray Diffraction Studies.* XRPD patterns were acquired on a Bruker D8 Discover diffractometer equipped with a Cu Kα source and a LynxEye silicon strip detector. Pt-functionalized UiO-67 MOFs were subjected to RT XRPD analysis; in all cases only diffraction peaks from the expected phase were measured, discarding the presence of undesired crystalline phases. Moreover, to test the thermal stability of the functionalized MOF (UiO-67-Pt(II)-PMLS), 100 mg of powder was heated in air for 2 h at 473, 573, 673, 723, and 773 K. A diffraction pattern was acquired between each cycle of heating. At 773 K, the MOF decomposed. On the crystalline phase of the premade $PtCl_2(H_2bpydc)$, $PtBr_2(H_2bpydc)$, $Pt(tdt)(H_2bpydc)$, and $PtBr_4(H_2bpydc)$ linkers, single crystal X-ray diffraction was measured at 100 K using a Bruker D8 Venture diffractometer with Mo Kα radiation (λ = 0.709 Å), see Supporting Information.

2.2.2. N$_2$ Adsorption Isotherms. The adsorption of nitrogen was measured gravimetrically at 77 K with a BELSORP-mini II instrument, and the specific surface area was obtained by the BET method. The samples were heated to 250 °C and kept at this temperature under continuous evacuation for 3 h prior to the adsorption measurement. The BET surface areas were calculated according to the principles outlined by Walton and Snurr.[40] N$_2$ adsorption isotherms confirmed that, with the only exception of UiO-67-Pt(II)_OPS sample, the Pt-functionalized UiO-67 materials basically kept the expected surface area and pore volume, as detailed in Table 1. Indeed, fluctuations up to 30% in the measured BET surface area (from 1105 to 1455 m^2 g^{-1}) can be ascribed to the absence of a fraction of the linkers connecting the Zr_6 inorganic cornerstones, as it has been recently shown for a set of different UiO-66 samples systematically synthesized by tuning both the synthesis temperature and the molar ratio between the linker and the Zr precursor.[41] Other authors have also played with the

Table 1. Summary of the BET Surface Area and Pore Volume of the Pt-Functionalized UiO-67 MOFs[b]

sample	A_s (m^2 g^{-1})	V_m (cm^3 g^{-1})	ref
UiO-67 theoretical value	2611	0.73	this work
UiO-67	1877	0.85	22
UiO-67	2504	1.01	this work
UiO-67(bpydc)	2252	0.92	this work
UiO-67-Pt(II) theoretical value[a]	2513	0.82	this work
UiO-67-Pt(II)_PMLS	2222	1.10	this work
UiO-67-Pt(II)_OPS	1504	0.63	this work
UiO-67-Pt(II)_PSF	2083	0.87	this work
UiO-67-Pt(II)_PSF_tdt	2450	1.11	this work
UiO-67-Pt(IV)_OPS	2399	0.98	this work
UiO-67-Pt(IV)_PMLS	1934	0.87	this work

[a]Theoretical value calculated of a 20% insertion of PtCl$_2$(H$_2$bpydc) in the framework [b]Theoretical values have been obtained using the Connolly algorithm[45] with a sphere of radius 1.84 Å.

modulation of the linker defectivity in UiO-66 material.[42,43] By varying the concentration of the acetic acid modulator and the synthesis time Wu et al.[42] obtained UiO-66 samples with pore volumes ranging from 0.44 to 1.0 cm^3 g^{-1} and BET surface areas ranging from 1000 to 1600 m^2 g^{-1}. Vermoortele et al.[43] used trifluoroacetic acid and HCl during the synthesis of UiO-66, resulting in a highly crystalline material, with partial substitution of terephthalates by trifluoroacetate. The latter were removed by thermal activation, resulting in a more open framework with a large number of open sites and a larger surface area than the perfect material, showing a higher activity in Lewis acid catalyzed reactions.[43] Also the Hf-UiO-66 homologue was found having a significant fraction of missing ligands.[44]

Coming back to the functionalized UiO-67 described in Table 1, although the one-pot synthesis method gives a crystalline product, both yields and porosity are poorly reproducible from this method. As far as sample UiO-67-Pt(II)_OPS is concerned, it is worth underlying that the OPS method with the Pt(II) precursor has shown to be quite critical. Investigations with SEM show that there is no discernible crystal morphology or homogeneous size dispersion in UiO-67-Pt(II)-OPS samples (see the Supporting Information). The MOF is likely formed along with another dense amorphous phase. Conversely, the OPS method gave excellent results when using Pt(IV) precursors.

2.2.3. TGA Experiments. Thermogravimetric analysis (TGA) was carried out in a Rheometric Scientific STA1500 instrument. Around 10 mg of the sample was placed in an Al$_2$O$_3$ crucible. The TGA profile was obtained by heating it from ambient temperature to 950 °C (heating rate 2 °C/min with continuous N$_2$ or H$_2$/N$_2$ flow). The instrument was equipped with a quadrupole mass spectrometer (MS) to investigate the chemical nature of the species leaving the sample in the TGA run. Experiments evidenced that, whatever is the adopted synthesis method, the Pt-functionalization of the MOF material does not compromise the high stability of the UiO-67 framework that showed the structure breakdown just above 773 K.[22]

2.2.3. IR Experiments. Infrared spectra were recorded at room temperature on a Bruker IFS 66 FTIR spectrometer, equipped with an MCT cryo-detector. Each reported spectrum has been obtained averaging 64 interferograms, recorded at 2 cm^{-1} resolution. MOFs samples were inspected in the form of thin self-supported pellets hosted inside a cell allowing *in situ* thermal activation and gas dosage to be made. Before measuring, MOFs were subjected to a H$_2$-reduction treatment at 650 K; then the sample was cooled down to 300 K and equilibrated with a CO equilibrium pressure (P_{CO}) of 30 mbar. Observed Pt-carbonyls were stable upon decreasing P_{CO} down to 10^{-3} mbar at RT; consequently, lower CO coverages were successively investigated by activating under vacuum the sample at increasing temperatures.

2.3. X-ray Absorption Experiments. XAS experiments were carried out at the beamline I811 of the MAX-II storage ring in Lund (Sweden),[46,47] operating at 1.5 GeV with a current ranging between 275 and 190 mA (2 injections per day). The white beam X-ray source of I811 is a 49-pole, liquid He-cooled superconducting wiggler (period = 65 mm). The beam was selected ($\Delta E/E \sim 10^{-4}$) by a horizontally sagitally focused double-crystal Si(111) monochromator detuned to 20% to minimize the third harmonic (around 35 keV); mirrors were not used in the adopted configuration. EXAFS spectra were collected in transmission mode at the Pt L$_3$-edge (11.56 keV) using a mixture of Ar and N$_2$ gases to guarantee 15 and 70% of absorption in the I_0 and I_1 ionization chambers, respectively.

Samples, in the form of self-supporting pellets of optimized thickness, were hosted inside an *ad hoc* cell[48] allowing sample activation, temperature setting or programming and atmosphere control either under static (*in situ* experiments) or dynamic (*operando* experiments) conditions.[36,49−62]

2.3.1. In Situ Static EXAFS Experiment. EXAFS spectra of samples in static conditions (desolvated MOFs and reference compounds) were collected at room temperature in the standard step-scan motion-mode of the monochromator[36] with the following sampling strategy: (i) from 150 to 30 eV before the edge the sampling step was $\Delta E = 5$ eV and the acquisition time was $\Delta t = 1$ s; (ii) from 30 to 15 eV before the edge $\Delta E = 1$ eV, $\Delta t = 1$ s; (iii) from 15 eV before to 40 eV after the edge $\Delta E = 0.25$ eV, $\Delta t = 1$ s; (iv) in the EXAFS region, from 40 to 1500 eV after the edge, corresponding to $k_{max} = 19.8$ Å^{-1}, a constant sampling step in k-space of $\Delta k = 0.025$ Å^{-1} was adopted with a Δt that linearly increases with k from 2 to 10 s.

The extraction of the $\chi(k)$ function was performed using the Athena code.[63] For each sample, 3 consecutive EXAFS spectra were collected, and corresponding $\chi(k)$ functions were averaged before data analysis.[64] EXAFS data analysis was performed using the Arthemis software.[63] Phase and amplitudes for the Pt−N and Pt−Cl single scattering paths were calculated by the FEFF6 code[65] using as input the structure of the crystalline PtCl$_2$(H$_2$bpydc) and PtCl$_4$(H$_2$bpydc)[66] solved by single crystal XRD and confirmed by ^{1}H NMR spectroscopy, see the SI. The validity of the Pt−N and Pt−Cl phase and amplitudes functions computed by the FEFF6 code[65] was further checked on K$_2$PtCl$_4$ and Na$_2$PtCl$_6$ model compounds. The averaged $k^3\chi(k)$ function were Fourier Transformed in the $\Delta k = (3.2−18.5)$ Å^{-1} interval. The fits were performed in R-space in the $\Delta R = 1.10−2.65$ Å range ($2\Delta k\Delta R/\pi > 15$).

2.3.2. Operando TPR-EXAFS Experiments. Operando temperature-programmed H$_2$-reduction (TPR) was performed feeding the sample with a flow of 10 cm^3 min^{-1} of 3% H$_2$ in He, hosted inside an *ad hoc* conceived cell allowing temperature control and *in situ* XAS measurements in flux to be done.[48,49] The H$_2$-TPR experiment was followed by EXAFS collecting the data in the quick-EXAFS scanning mode of the monochromator, i.e. with a continuous motion of the Bragg angle of the monochromator with a progressive reading of I_0 and I_1 currents.[36] The rotation/translation speed of the monochromator was set to allow the collection of an EXAFS spectrum from −100 to +800 eV from the edge (corresponding to $k_{max} = 14.5$ Å^{-1}) in 360 s (back motion included). As the heating ramp of the TPR was 3 K min^{-1}, EXAFS spectra were recorded with a temperature resolution of 18 K. The investigated temperature range was 300−745 K, resulting in a series of 25 correlated EXAFS spectra.

The Athena code[63] was used also for the extraction of the $\chi(k)$ functions of the spectra collected during the TPR experiments. However, in this case we used the IFEFFIT[67] code that allows to perform the parametric EXAFS data analysis on the whole set of spectra of a given experiment. We used the same phases and amplitudes functions used to model the Pt−N and Pt−Cl single scattering in the analysis of the static EXAFS spectra. Extracted $k^3\chi(k)$ function were Fourier transformed in the $\Delta k = 3.20−11.50$ Å^{-1} interval. The fits were performed in R-space in the $\Delta R = 1.10−2.65$ Å range ($2\Delta k\Delta R/\pi > 8$).

The main goal of the TPR-EXAFS experiment was to provide the temperature dependence of both N_N and N_{Cl} coordination numbers in order to establish whether a temperature range allowing to break the Pt−Cl bonds without breaking the Pt−N ones exists or not. The major difficulty in achieving this goal was related with the strong correlation among coordination numbers (N_N, N_{Cl}) and Debye−Waller factors

$(\sigma^2_N, \sigma^2_{Cl})$ in an experiment where the latter are not constant but increase progressively along the series of spectra because of the increase of the temperature T. In the literature there are some accurate studies modeling the Debye−Waller factors of the different EXAFS paths as a function of the vibrational density of states.[68−73] In particular, the Debye or the Einstein[74] model has been adopted to predict the dependence of the σ^2 factors with the temperature.[75−86] For all the TPR-EXAFS experiments, but UiO-67-Pt(IV)_PMLS, the following procedure, based on a four steps-refinement, has been adopted.

First Refinement Step. Each EXAFS spectrum of the series has been analyzed independently from the others, refining a unique ΔE, the two coordination numbers (N_N and N_{Cl}), and the two Debye−Waller factors (σ^2_N and σ^2_{Cl}), while the bond distances ($R_{Pt−N}$ and $R_{Pt−Cl}$) have been fixed to the values obtained in the refinement of the EXAFS spectrum collected in static conditions at RT in a higher k-range before starting the TPR experiment. This constrain was imposed to avoid the fit instabilities observed for the high-temperature spectra. Indeed, when the loss of chlorine starts to be important, resulting in $N_{Cl} < 1.0$, then the Cl-shell has the tendency to merge with the N-shell, with an obviously nonphysical result. The main drawback of this constrain is related to the fact that we cannot follow directly the expected thermal bond elongation. This is however a minor problem as the main goal of this study is to determine the temperature range able to remove the Cl ligands, without extracting the platinum from the MOF framework. Actually, the thermal expansion is roughly taken into account in the fit by optimizing a unique ΔE factor, which strongly correlates with the bond distances. Along all series, the optimized ΔE values differ by slightly less than 1 eV, resulting in $\Delta R_{Pt−N} < 0.005$ Å and $\Delta R_{Pt−Cl} < 0.004$ Å. Plotting the results of N_N, N_{Cl}, σ^2_N, and σ^2_{Cl} vs T obtained after the first refinement step, the optimized values start to lose physical meaning starting from a given temperature (T_c), resulting in negative σ^2 or unphysical N values, see below Figure 7a. In the different experiments T_c was found in the 640−670 K range.

Second Parametric Refinement Step. Working on the subset of data in the interval between RT and (T_c-20) K, we have then performed a parametric refinement, commonly adopted in XRPD Rietveld refinements,[87,88] of the spectra of each TPR-EXAFS series adopting the Einstein model for describing the temperature dependence of both σ^2_N and σ^2_{Cl} factors. The Einstein model approximates the vibrational density of states as a Dirac delta function spiked at a single frequency named Einstein frequency (ω_E). The model assumes that the pair Pt−N (or Pt−Cl) behaves as a quantum harmonic oscillator of mass equal to the reduced mass of the atomic pair ($M = 13.070$ and 30.004 amu for the Pt−N and Pt−Cl pairs, respectively). Under such assumptions, the $\sigma^2(T)$ behavior is straightforwardly determined by the only ω_E parameter according to the equation[85]

$$\sigma^2(T) = \frac{\hbar}{M\omega_E} \cot gh\left[\frac{\hbar\omega_E}{2k_BT}\right] = \frac{\hbar^2}{Mk_B\Theta_E} \cot gh\left[\frac{\Theta_E}{2T}\right] \quad (1)$$

Being Θ_E is the Einstein temperature of the Pt−N (or Pt−Cl) bond, related to the Einstein frequency by the relationship: $\hbar\omega_E = k_B\Theta_E$, where $\hbar = 1.055 \times 10^{-34}$ J s is the reduced Plank constant and $k_B = 1.38 \times 10^{-23}$ J K^{-1} is the Boltzmann constant.

The adopted parametric refinement consists in the simultaneous refinement of the ~20 EXAFS spectra collected in the interval between RT and (T_c-20) K, using independent ΔE, N_N, and N_{Cl} parameters for each spectrum plus two Θ_E temperatures that allowed to parametrize $\sigma^2_N(T)$ and $\sigma^2_{Cl}(T)$ according to eq 1. This approach allowed us to reduce the number of parameters used to optimize the thermal factors of the series from ~40 to 2, with a consequent reduction of the correlation among the optimized parameters and thus a reduction of the relative error bars. In such a way, we obtain the Einstein temperatures (Θ_E) for both Pt−N and Pt−Cl oscillators, that allows us to obtain a straightforward dependence of both σ^2_N and σ^2_{Cl} vs T, that can be extrapolated on the whole set of data (i.e., also above T_c). The Θ_E values obtained in this way are subjected to an error of 10−15%, mainly owing to the superimposition of the damping effect due to an increase of the thermal disorder and to the loss of the first Cl and N ligands, close to T_c.

Third Parametric Refinement Step. A significant improvement in the Θ_E values optimization is obtained by further decreasing the temperature interval of the parametric refinement to the (RT-473 K) one, where from the previous fits both N_N and N_{Cl} are compatible with the ideal value of 2. This approach is supported by the fact that the EXAFS spectrum collected on a pellet of UiO-67-Pt(II)_PMLS MOF heated up just to 473 K in H$_2$/He flow and successively cooled down to room temperature was virtually equivalent to the EXAFS spectrum collected on the same pellet before the heating treatment. This blank experiment testifies that there is no significant loss of ligands in the RT-473 K interval.

Fixing $N_N = N_{Cl} = 2$ and running again the parametric fit on this subset of TPR-EXAFS spectra we better isolated the thermal effect on the intensity of the EXAFS signal and we obtained Θ_E values accurate below 10% for σ^2_N and below 3% for σ^2_{Cl}. This achievement is very important to reduce the final error on $\sigma^2(T)$ that propagates from the error on Θ_E through eq 1. The obtained Einstein temperatures Θ_E for both Pt−N and Pt−Cl bonds are reported in Table 2.

Table 2. Summary of the Einstein Temperatures Θ_E Obtained for Both Pt−N and Pt−Cl Bonds in the Temperature-Dependent EXAFS Experiments[a]

sample	Θ_E(Pt−N) (K)	Θ_E(Pt−Cl) (K)
PtCl$_x$(H$_2$bpydc) linker	912 ± 90	434 ± 12
UiO-67-Pt(II)_PMLS	709 ± 63	333 ± 9
UiO-67-Pt(IV)_PMLS	709 ± 63	333 ± 9

[a]The higher is Θ_E, the lower is the corresponding σ^2 value, at any T, see eq 1. As discussed in the text, for UiO-67-Pt(IV)_PMLS the Einstein temperatures were assumed to be the same as for UiO-67-Pt(II)_PMLS.

Fourth, and Final, Refinement Step. It consists in analyzing again the whole series of EXAFS spectra with independent fits for each spectrum (no parametric fit) where we optimize only a unique ΔE and the two coordination numbers (N_N and N_{Cl}), being the two Debye−Waller factors (σ^2_N and σ^2_{Cl}) fixed to the value obtained from eq 1 and from the Θ_E parameters determined in the third refinement step. For the result of this final refinement, *vide infra* Figure 7(b)-(d).

For sample UiO-67-Pt(IV)_PMLS the third step of this strategy was not feasible because, under H$_2$ flow, Pt atoms started losing Cl ligands already at room temperature. As the Einstein temperatures determined in the second refinement step for both Pt−N and Pt−Cl bonds were close to those obtained for sample UiO-67-Pt(II)_PMLS, in this case we decided to run the fourth step of the refinement adopting the Θ_E values refined for the UiO-67-Pt(II)_PMLS material.

2.4. Resonant Inelastic X-ray Scattering. Valence-to-core resonant inelastic X-ray scattering (RIXS) experiments[38,89−91] were performed at the European Synchrotron Radiation Facility (ESRF) using the high brilliance spectroscopy beamline ID26.[92] The storage ring current was between 200 mA and 170 mA. The energy of the incident photon beam ($\hbar\Omega$) was selected using the (311) reflection of a pair of cryogenically cooled Si single crystals. Higher harmonics were suppressed adopting two mirrors with a Pd/Cr coating operating in total reflection at 2.7 mrad. The total X-ray flux at the Pt L$_3$-edge was 4.87×10^{12} photons s^{-1} as determined by measuring the current on a Canberra photodiode. The beam size was approximately 600 μm horizontal and 100 μm vertical. The X-ray spectrometer developed at ID26 was used to select the energy of the photons emitted by the samples ($\hbar\omega$). It was equipped with spherically bent (radius = 1 m) Si(933) crystal analyzers. The selected photons were detected by means of an avalanche photodiode (APD) with an active area of 10 × 10 mm^2 and a thickness of the Si layer of 200 μm. The full width at half-maximum of the elastic peak was about 1.4 eV (instrumental bandwidth). Radiation damage tests revealed no effect of the beam on the samples.

Table 3. Summary of the Fits Performed on the Static EXAFS Spectra Collected at RT on the PtCl$_2$(H$_2$bpydc) Linker and on the UiO-67-Pt(II) MOFs Synthesized Following Different Methods (see Section 2.1)^a

sample	shell	N	σ^2 (Å^2)	R (Å)	E_0 (eV)	S_0^2	R-factor
PtCl$_2$(H$_2$bpydc)	Pt–N	2	0.002 ± 0.001	2.02 ± 0.01	0 ± 2	0.92 ± 0.09	0.016
linker	Pt–Cl	2	0.0028 ± 0.0007	2.304 ± 0.007			
UiO-67-Pt(II)_PMLS	Pt–N	2.0 ± 0.3	0.002 ± 0.001	2.02 ± 0.01	1 ± 2	0.92	0.016
	Pt–Cl	2.2 ± 0.2	0.0028 ± 0.0008	2.297 ± 0.006			
UiO-67-Pt(II)_OPS	Pt–N	1.9 ± 0.3	0.003 ± 0.001	2.02 ± 0.01	1 ± 2	0.92	0.017
	Pt–Cl	2.3 ± 0.2	0.0029 ± 0.0009	2.302 ± 0.08			
UiO-67-Pt(II)_PSF	Pt–N	2.0 ± 0.3	0.002 ± 0.001	2.02 ± 0.01	1 ± 2	0.92	0.023
	Pt–Cl	1.8 ± 0.2	0.0025 ± 0.0006	2.295 ± 0.008			

$^a\Delta k = (3.2–18.5)$ Å^{-1}; $\Delta R = (1.10–2.65)$ Å. Underlined numbers refer to not optimized parameters. The graphical quality of the fit as well as the different contribution of the N and Cl ligands can be appreciated in Figure 3 for sample UiO-67-Pt(II)_PSF in both R- and k-spaces.

3. RESULTS AND DISCUSSION

The aim of this work is threefold. First, we want to prove that the different synthesis methods succeeded in inserting Pt atoms in the desired framework position with the desired chemical environment. Subsequently, we will prove that it is possible, in a H$_2$-TPR experiment, to remove almost all Cl ligands from the first coordination shell of Pt, leaving the Pt–N bonds almost unaffected, i.e. that it is possible to have a significant fraction of Pt species grafted to the UiO-67 framework with coordinative unsaturation for possible catalytic applications. The former point will be debated in Section 3.1, the latter in Section 3.2. Finally, we will investigate by XAS the reactivity of a selected parent UiO-67-Pt(II) MOF toward thiol and Br$_2$, as it will be discussed in Section 3.3.

3.1. Determination of the Pt Local Environment. *3.1.1. EXAFS.* The EXAFS refinement of the PtCl$_2$(H$_2$bpydc) linker, used as a model compound to verify the validity of phase and amplitude functions computed by FEFF6 code,[65] was satisfactory. Indeed, it was able to reconstruct both R_{Pt-N} and R_{Pt-Cl} given by single crystal diffraction (2.0095 and 2.2935 Å, respectively, see the SI), as reported in Table 3. The same holds for the amplitude, because fixing the coordination numbers to the expected values ($N_{Pt-N} = N_{Pt-Cl} = 2$) we obtained an amplitude reduction factor S_0^2 close to unit[36,72,91,93,94] (0.92 ± 0.09), together with meaningful Debye–Waller factors, see Table 3. This result allowed us to fix $S_0^2 = 0.92$ in all the fits performed on the different UiO-67-Pt MOFs.

The analysis on samples UiO-67-Pt(II)_PMLS, UiO-67-Pt(II)_OPS, and UiO-67-Pt(II)_PSF was straightforward, see Table 3. It resulted in a Pt(II) environment perfectly compatible with that of platinum in the PtCl$_2$(H$_2$bpydc) linker, testifying that all three synthesis methods resulted in a structure compatible with target UiO-67-Pt(II) MOF reported in the right-hand term of the reaction schematized in Figure 2. The quality of the obtained fits can be appreciated in Figure 3, parts (a) and (c) for the R- and k-spaces, respectively, for the UiO-67-Pt(II)_PSF case.

Parts (b) and (d) of Figure 3 show the differences between the Pt–N and Pt–Cl contributions in the R- and k-spaces, respectively, and are useful to discuss the ability (and the limitations) of the technique to differentiate among them. In the phase uncorrected R-space the maxima of the two components are well separated, being centered at 1.66 Å (Pt–N) and at 1.95 Å (Pt–Cl), but their overall contributions are partially overlapped (top spectra in Figure 3b). This implies that it is impossible to fit separately the two components and that a decrease in the intensity of one component (due either to an increase of σ^2, or to a decrease of N, or both) will influence
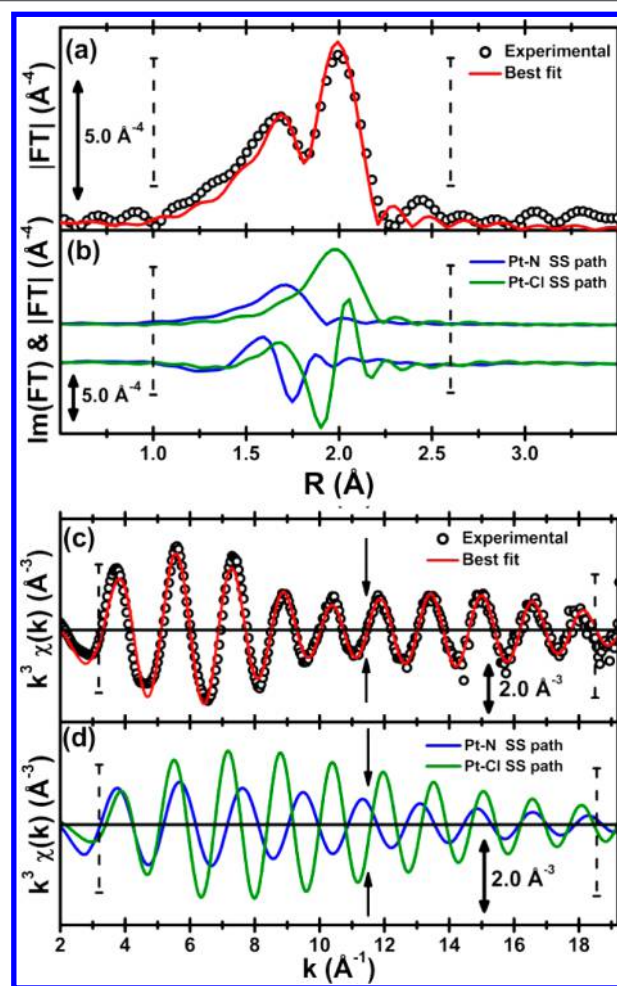
Figure 3. Summary of the EXAFS analysis performed on UiO-67-Pt(II)_PSF: spectrum collected at RT in static conditions, before starting the TPR experiment. Part (a): comparison between the k^3-weighted, phase uncorrected, FT of the experimental signal (black circles) and the corresponding best fit (red curve). Part (b): comparison, in R-space, between the Pt–N (blue curve) and Pt–Cl (green curve) SS contributions. Both moduli (top) and imaginary parts (bottom) have been reported. Part (c): as part (a) in the k-space. Part (d): as part (b) in the k-space. Vertical dashed lines define the intervals in k- and R-spaces used to perform the fit of all data collected at RT in static conditions. The two vertical arrows in part (d) indicate the upper limit of the k-space used to fit the time-resolved TPR-EXAFS data (*vide infra* Section 3.2.2). The quantitative results of the fit are reported in Table 3.

Table 4. Summary of the Fits Performed on the Static EXAFS Spectra collected at RT on the PtCl$_4$(H$_2$bpydc) Linker and on the UiO-67-Pt(IV) MOFs Synthesized Following Different Methods (see Section 2.1)^a

sample	shell	N	σ^2 (Å^2)	R (Å)	E$_0$ (eV)	S$_0^2$	R-factor
PtCl$_4$(H$_2$bpydc)	Pt–N	2	0.003 ± 0.001	2.04 ± 0.01	0 ± 1	0.93 ± 0.06	0.0085
linker	Pt–Cl	4	0.0027 ± 0.0004	2.311 ± 0.004			
UiO-67-Pt(IV)_OPS	Pt–N	2	0.0009 ± 0.0007	2.01 ± 0.01	1 ± 1	0.68 ± 0.06	0.0117
Fit-a (preliminary)	Pt–Cl	4	0.0032 ± 0.0005	2.303 ± 0.005			
UiO-67-Pt(IV)_OPS	Pt–N	2.1 ± 0.3	0.0026 ± 0.0004	2.02 ± 0.01	1 ± 1	0.92	0.0085
Fit-b (preliminary)	Pt–Cl	2.6 ± 0.3	0.0026 ± 0.0004	2.306 ± 0.005		0.92	
UiO-67-Pt(IV)_OPS	Pt–N	2	0.002 ± 0.001	2.02 ± 0.01	1 ± 1	0.92	0.0080
Fit-c (final)	Pt–Cl	2.7 ± 0.3	0.0026 ± 0.0005	2.305 ± 0.005		0.92	
UiO-67-Pt(IV)_PMLS	Pt–N	2	0.0012 ± 0.0006	2.024 ± 0.009	1 ± 1	0.71 ± 0.05	0.0097
Fit-a (preliminary)	Pt–Cl	4	0.0030 ± 0.0004	2.307 ± 0.004			
UiO-67-Pt(IV)_PMLS	Pt–N	2.4 ± 0.8	0.0021 ± 0.0006	2.03 ± 0.01	1 ± 1	0.92	0.0058
Fit-b (preliminary)	Pt–Cl	2.4 ± 0.4	0.0021 ± 0.0006	2.309 ± 0.004		0.92	
UiO-67-Pt(IV)_PMLS	Pt–N	2	0.0029 ± 0.0006	2.056 ± 0.009	1 ± 1	0.92	0.0063
Fit-c (final)	Pt–Cl	2.6 ± 0.2	0.0024 ± 0.0003	2.312 ± 0.004		0.92	

$^a\Delta k = (3.2–18.5)$ Å^{-1}; $\Delta R = (1.10–2.65)$ Å. For the two UiO-67-Pt(IV) MOFs three different refinements have been tried before reaching the final one. Besides R_N, R_{Cl}, and E_0, refined in all fits, **Fit-a** keeps N_N and N_{Cl} fixed to the expected stoichiometric for the PtCl$_4$(H$_2$bpydc) linker and refines S_0^2, σ^2_N, and σ^2_{Cl}. **Fit-b** fixes S_0^2 to the best fit value obtained for UiO-67-Pt(II)_MOFs ($S_0^2 = 0.92$), equivalent within the experimental errors to that obtained from the fit of the PtCl$_4$(H$_2$bpydc) linker and leaves both N_N and N_{Cl} free; for stability reasons a single σ^2 factor, common to both shells, was refined. **Fit-c** fixes N_N to 2 and S_0^2 to 0.92, refining N_{Cl} and two independent σ^2_N and σ^2_{Cl} Debye-Waller factors. In all cases, underlined numbers refer to not optimized parameters.

the R-region dominated by the second and *vice versa*. The differences between the two contributions are better appreciated looking to the imaginary parts of the FT (bottom spectra in Figure 3b). The two components are (i) negligible below 1.3 Å; (ii) in phase in the (1.30–1.65) Å interval; (iii) in negative interference in the (1.65–1.95) Å region; (iv) while in the (1.96–2.65) Å region only the Pt–Cl signal contributes significantly. In k-space (Figure 3d), the two signals are in phase up to $k \sim 6.7$ Å^{-1}, they are in opposition of phase in the (~ 6.7–13.1) Å^{-1} interval, becoming again in phase from ~13.1 Å^{-1} to ~19.2 Å^{-1}. These considerations explain the behavior of the experimental datum (Figure 3c), showing first a rapid decrease in intensity, which stops around $k \sim 12$ Å^{-1}. The apparently "unnatural" invariance of the oscillation intensity in the $k \sim$ (12–16) Å^{-1} region (showing even a slight increase in the (14–16) Å^{-1} range) is so explained by the fact that the Pt–N and Pt–Cl contributions come back in phase in that region. The significant difference in the integrated intensities of the two signals (due to the different scattering power of the two atoms: $Z = 7$ and 17 for N and Cl, respectively) prevents the observation of a well-defined beat and generated just a modulation in the EXAFS amplitude that has a periodicity in k-space that in the first approximation is given by $\pi/[2\Delta R] \sim 6.3$ Å^{-1},[36] where $\Delta R = R_{Pt–Cl} − R_{Pt–N} \sim 0.25$ Å.

The adopted sampling strategy and related fit intervals adopted in both the static (up to $k_{max} = 18.5$ Å^{-1}, see dashed vertical bars in Figure 2) and in the TPR (up to $k_{max} = 11.5$ Å^{-1}, see full vertical arrows in the same figure) experiments guarantee a sufficiently large k-interval to be safely able to discriminate between Pt–N and Pt–Cl contributions because they cover k-regions where the two signals are either in phase or in opposition of phase, see Figure 3d.

Phase and amplitude functions computed by the FEFF6 code[65] were further checked in the refinement of the PtCl$_4$(H$_2$bpydc) linker. Also in this case it was possible to reconstruct both $R_{Pt–N}$ and $R_{Pt–Cl}$ given by XRPD (2.05 and 2.31 Å, respectively),[66] see Table 4. The same holds for the amplitude, because fixing the coordination numbers to the

expected values ($N_{Pt–N} = 2$; $N_{Pt–Cl} = 4$) we obtained an S_0^2 factor close to unit[36,72,91,93] (0.93 ± 0.06), together with meaningful Debye−Waller factors, see the first two lines in Table 4.

The analysis on both UiO-67-Pt(IV)_PMLS and UiO-67-Pt(IV)_OPS samples was much more delicate than that discussed so far for their Pt(II) homologues, see Table 3. We first tried the strategy successfully tested on the Pt(II) homologues (**Fit-a** in Table 4), that however failed. Indeed, fixing the coordination numbers to the expected values $N_N = 2$ and $N_{Cl} = 4$, the fit resulted in a physically too low S_0^2 factor (in the 0.68−0.71 range) and in a physically unreasonable, almost null, σ^2_N factor (in the 0.0009−0.0012 Å^2 range). A so low S_0^2 factor implies that the model overestimates both coordination numbers or, at least, the coordination number related to the most intense Pt–Cl signal. Based on the fact that $S_0^2 = 0.92$ resulted in a reasonable optimization of the stoichiometry for the Pt(II) homologues (see Table 3), in **Fit-b** we fixed S_0^2 to 0.92 (for consistency with the fits performed on Pt(II) complexes and in agreement with the value found on the PtCl$_4$(H$_2$bpydc) linker), allowing N_N and N_{Cl} to vary independently. To avoid fit instabilities, we were forced to optimize a unique Debye−Waller factor common for both Pt–N and Pt–Cl bonds. The results of the fit (see Table 4) were compatible with $N_N = 2$ but pointed out N_{Cl} values significantly lower than 4. This explains the mathematical results of **Fit-a**, where $\sigma^2_N \sim 0$ compensated the low S_0^2 factor forced by a too high fixed N_{Cl} value. From what has been learned from the first two refinements, we were able to run the final one (**Fit-c** in Table 4), where we fixed $S_0^2 = 0.92$ and $N_N = 2$, refining N_{Cl} and two independent σ^2_N and σ^2_{Cl} factors. For both UiO-67-Pt(IV)_PMLS and UiO-67-Pt(IV)_OPS samples, a value $N_{Cl} \sim 2.6$ was observed, implying that during the synthesis procedure, both the PMLS and the OPS one, about 70% of the Pt(IV) species are reduced to Pt(II), losing two out of the four chlorine ligands.

3.1.2. RIXS. Results from EXAFS (see above Section 3.1.1) showed that the local environment of the Pt(II) species in Pt-

functionalized UiO-67 samples prepared via OPS, PMLS, and PSF methods is the same as that in the PtCl$_2$(H$_2$bpydc) linker. Such evidences are further confirmed by RIXS.

Pt-L$_3$ RIXS planes of the UiO-67-Pt(II)_PMLS MOF and of the PtCl$_2$(H$_2$bpydc) linker were collected by scanning the edge peak of the XANES spectrum (top spectra in Figure 4a,b) and
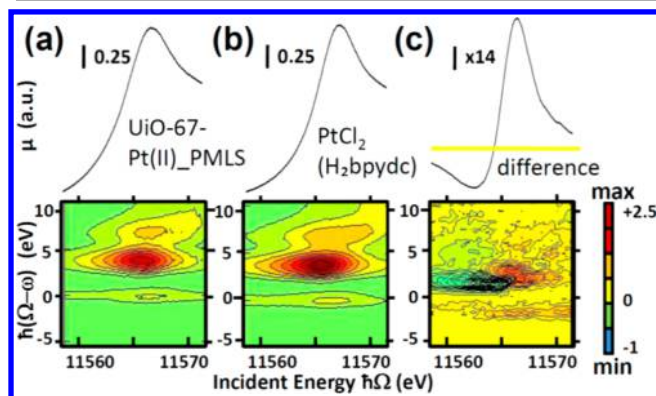

Figure 4. Part (a): Total fluorescence yield (TFY) XANES spectrum (top) and RIXS map of UiO-67-Pt(II)_PMLS. The latter reports the intensity of the X-ray fluorescence emitted by the sample as a function of both the incident energy ($\hbar\Omega$) and the energy transferred to the sample $\hbar(\Omega-\omega)$, allowing to obtain a complete insight on both occupied and unoccupied electronic density of states.[38,89,91] Part (b): as part (a) for the premade PtCl$_2$(H$_2$bpydc) linker. Part (c): difference TFY spectra (top) and RIXS map (bottom) highlighting the minor, but measurable, effects on the Pt(II) electronic configuration upon insertion of the PtCl$_2$(H$_2$bpydc) linker into the UiO-67 framework. The yellow horizontal line in the top part represents the zero level of the difference spectrum. The color code on the right quantifies the intensities of the three RIXS maps.

covering an energy transfer $\hbar(\Omega-\omega)$ up to 11 eV, hence exploring the valence-to-core transitions region. As a reference to obtain the zero value on the energy transfer axis, $\hbar(\Omega-\omega)$ ordinate axis, we used the elastic peak, measured scanning the energy of the fluorescence photon ($\hbar\omega$) while keeping the incident energy ($\hbar\Omega$) fixed. The maps of both the UiO-67-Pt(II)_PMLS MOF and the PtCl$_2$(H$_2$bpydc) linker show three main features (bottom parts in Figure 4a,b). The feature at $\hbar(\Omega-\omega)$ = 0 eV is the elastic peak and is not informative, while the ones at high energy transfer $\hbar(\Omega-\omega)$ = 3.7 and 7.0 eV reflect the Pt-projected valence electronic structure of the systems under investigation. These two features are mainly linked to electronic levels originating from the mixing of the Pt(5d) and Cl(3p) atomic electronic levels. We observe that the RIXS map of the MOF is very similar to the one of the linker (bottom parts of Figure 4a,b), i.e. the Pt-projected valence band of the linker does not present significant variation when it is inserted within the MOF. This represents an important additional evidence that the local environment of the Pt(II) species in Pt-functionalized UiO-67 samples is very similar to that in the PtCl$_2$(H$_2$bpydc) linker. It is however worth noticing that, if we subtract the RIXS map of linker to that of the UiO-67-Pt(II)_PMLS MOF (see Figure 4c), small variations are appreciated. A qualitative interpretation of the slight modifications of the electronic structure presented in the difference map of Figure 4c can be obtained by considering the environment of the linker within the MOF framework. A more quantitative explanation requires sophisticated DFT calcula-

tions, as done elsewhere,[95,96] that are however outside the aim of the present work.

3.2. Thermal Stability at Long and Local Scales.
3.2.1. XRPD. The materials were tested for thermal stability by heating the powders in an open crucible for 2 h, measuring XRPD between each round of heating. The dry MOF powder was mounted on a glass plate XRPD sample holder wrapped with plastic foil, resulting in a broad plastic diffraction peak at 22°. The resulting patterns reveal that the material decomposes if heated to between 720 and 770 K in air, see Figure 5 for the
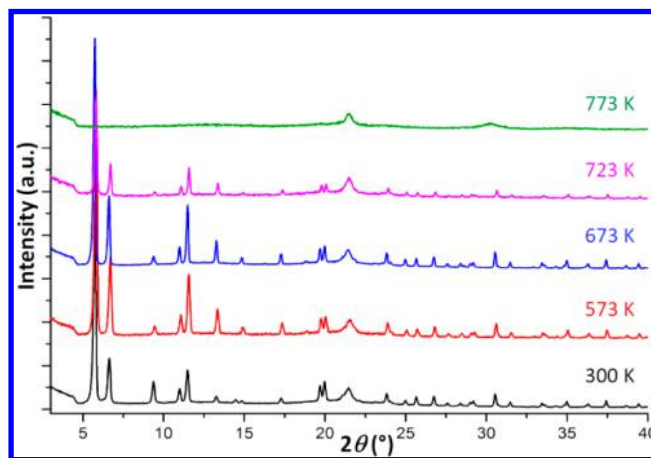

Figure 5. Evolution of the XRPD pattern of sample UiO-67-Pt(II)_PMLS, as a function of the temperature in air. The framework structure is stable up to 673 K. At 723 K a significant fraction of the MOF is still crystalline. At 773 K the structure collapses. The broad reflection around 2θ = 22° is due to the window of the cell. λ = 1.541 Å. Patterns were vertically shifted for sake of clarity.

UiO-67-Pt(II)_PMLS sample. The results are similar whether the material is functionalized or not and independently on the adopted functionalization method, OPS, PMLS, or PSF. The temperature-dependent XRPD study reported in Figure 5 clearly indicates that the framework structure of the function-alized UiO-67-Pt MOF is fully stable up to 673 K; at 723 K there is still an important fraction of crystalline phase, while the pattern collected at 773 K is typical of a fully amorphous phase, testifying the collapse of the MOF structure.

Due to the relatively low occupancy of the functionalized linkers vs the standard ones (1:9), the maintenance of the long-range-order testified by the XRPD experiment shown in Figure 5 gives no guarantee on the stability of the Pt species grafted to the MOF framework, neither on the eventual loss of Cl ligands. In order to provide answers to such questions the temperature dependent experiment has been repeated exploiting the element selectivity of the EXAFS technique and its local sensitivity.

3.2.2. TPR-EXAFS. Figure 6a reports the evolution of the Pt L$_3$-edge XANES spectra along the operando TPR experiments on UiO-67-Pt(II)_PMLS MOF. A small, but significant, loss of intensity of the edge intensity (technically named "white-line"[36]) together with a significant smoothing of the near edge-features are observed. These changes will be interpreted at the end of this section.

Figure 6b-d reports, in the R space, the sequence of EXAFS spectra collected as a function of the temperature on the PtCl$_2$(H$_2$bpydc) linker (part b) and on selected UiO-67-Pt(II)_PMLS, and UiO-67-Pt(IV)_PMLS MOFs, parts (c) and (d),
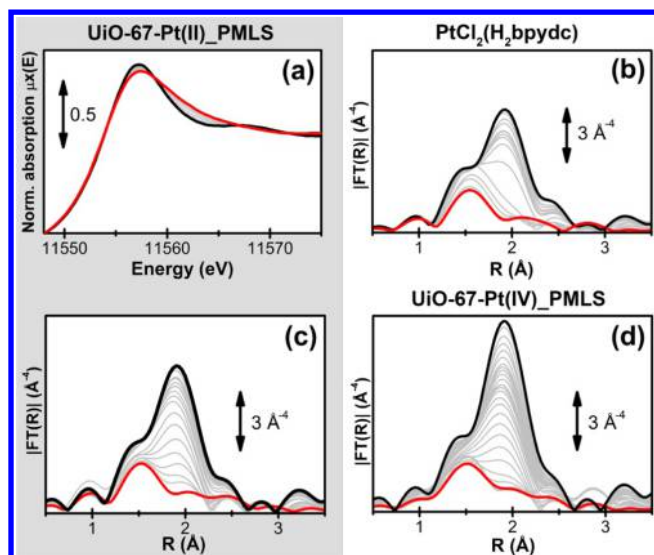
Figure 6. Part (a): Pt L_3-edge, XANES spectra collected during the operando TPR experiments on UiO-67-Pt(II)_PMLS MOF. The black spectrum has been collected at 300 K, the red one at 745 K, gray spectra refer to intermediate temperatures. Parts (b)-(d): k^3-weighted, phase uncorrected, FT of Pt L_3-edge EXAFS spectra collected during the operando TPR experiments on PtCl$_2$(H$_2$bpydc) linker (b) and on UiO-67-Pt(II)_PMLS (c), and UiO-67-Pt(IV)_PMLS (d) MOFs (same color code). Experiments were performed adopting a temperature gradient of 3 K min^{-1}. For graphical reasons, in parts (b)-(d), only a fraction of the collected spectra is reported. The quantitative data analysis of the set of spectra shown in parts (b)-(d) is reported in Figure 7(b)-(d), respectively.

respectively. Both Pt−N and Pt−Cl contributions, centered around 1.5 and 1.9 Å (without phase correction), undergo a progressive intensity decrease upon increasing the temperature under H$_2$ flow.

In all cases, the component due to Pt−Cl is clearly decreasing much faster than the Pt−N one. In order to determine the temperatures at which Pt−Cl and Pt−N bonds start to be cleaved, we have performed on the three sets of data the sophisticated parametric analysis described in section 2.3.2.

As discussed above, this loss of signal is due to both the progressive increase of the Debye−Waller factors (σ^2_N and σ^2_{Cl}) with the increasing temperature and, starting from a given temperature, to the possible progressive cleavage of Pt−N and Pt−Cl bonds, resulting in a possible decrease of N_N and N_{Cl}. To quantify the values of σ^2_N, σ^2_{Cl}, N_N, and N_{Cl} for the whole set of spectra reported in Figure 6 with the best accuracy possible and the minimal relative correlation, we adopted the sophisticated and demanding 4-steps analysis procedure described in Section 2.3.2. For the three EXAFS-TPR experiments shown in Figure 6b-d, the evolution vs T of the σ^2_N, σ^2_{Cl}, N_N, and N_{Cl} parameters obtained with this method is reported in Figure 7b-d.

For the PtCl$_2$(H$_2$bpydc) linker (Figure 7b), within the experimental errors, both N_N and N_{Cl} coordination numbers are stable to the stoichiometric values of 2.0 up to 600 K. At 620 K N_{Cl} starts to rapidly decrease, approaching zero at about 720 K. Conversely, N_N is stable until 660 K and then starts to decrease with a much lower slope resulting in N_N = 1.3 at 750 K. This means that in the 600−660 K interval the H$_2$ flow is able to break most of the Pt−Cl bonds (N_{Cl} = 0.4 at 660 K) removing the chlorine as HCl, keeping intact the Pt−N bonds with the bpydc rings. At temperatures higher than 660 K also

the Pt−N bonds start to break; nevertheless at 750 K a significant fraction of Pt(II) is still bound to the bpydc unit.

The EXAFS TPR experiment performed on the UiO-67-Pt(II)_PMLS MOF (Figure 7c) yield to the same trends, with minimal differences in the temperature intervals of stability of the two bonds. Both N_N and N_{Cl} are stable to the stoichiometric values of 2.0 up to 575 K, when they start to decrease together. However, while N_{Cl} decreases almost linearly to 0.4 at 750 K, N_N undergoes a fast decrease to 1.6 at 610 K and then remains almost stable, being its value at 750 K of 1.4. This means that a prolonged activation in H$_2$ of the UiO-67-Pt(II)_PMLS MOF in the 610−640 K interval will result in a minimal loss of Pt(II), that will lose the Pt−N connection with the framework, but in the break of an important fraction of the Pt−Cl bonds. This experiment proves that this activation temperature interval is ideal to obtain a material where most of the functionalized Pt(II) species are still linked to the MOF framework, exhibiting the coordination vacancies needed to make the UiO-67-Pt(II)_PMLS material a potential heterogeneous catalyst.

The material UiO-67-Pt(IV)_PMLS behaves differently in the EXAFS-TPR experiment, see Figure 7d. The Pt−N bond exhibits the same stability interval (RT−575 K) observed in experiment on UiO-67-Pt(II)_PMLS and then N_N progressively decreases until 1.25 at 750 K. Conversely, the Pt−Cl bond has no stability plateau. N_{Cl} shows a continuous decrease along the whole experiment exhibiting two different slopes in the RT−575 and 575−750 K intervals. In the former the slope is lower moving N_{Cl} from 2.5 to 2.0 ($\Delta N/\Delta T = -1.8 \times 10^{-3}$ K^{-1}), in the latter the slope is much higher, as N_{Cl} moves from 2.0 to 0.4 ($\Delta N/\Delta T = -9.1 \times 10^{-3}$ K^{-1}). This is clearly visible in the data reported in Figure 7d. As already discussed at the end of section 3.1.1, during the synthesis process only a minor fraction of platinum (about 30%) maintains the oxidation state (IV) and its four starting Cl ligands, whereas the remaining 70% is reduced to Pt(II), losing two out of the four chlorine ligands (Table 4). During the first heating step, from 300 to 575 K, all the Pt(IV) species lose two axial Cl ligands becoming square planar Pt(II) species with two nitrogen and two chlorine ligands. At that stage, they behave, in first approximation, as the parent Pt(II) species in the UiO-67-Pt(II)_PMLS MOF (Figure 7c)

Summarizing, for all investigated MOFs, including UiO-67-Pt(II)_OPS (see the Supporting Information), we observe in the 600−700 K range a significant loss of Cl$^-$ ligands and a minimal cleavage of Pt−N bonds. On a simple stoichiometric ground, the loss of two negatively charged Cl$^-$ ligands, leaving as neutral HCl molecules according to the reaction path bpydcPtCl$_2$ + H$_2$ → bpydcPt + 2HCl, is supposed to formally reduce Pt(II) to Pt^0. This hypothesis has been checked by XANES (Figure 6a), that is one of the most informative techniques in the determination of the oxidation state of a selected element.[36,38,91,97] Unlikely K-edge spectra, where the change in the oxidation state is mainly observed as a shift of the edge position,[36,49,98] L_3-edge XANES will show a very small edge shift[35,56] and is mainly influenced by a variation of the intensity of the "white-line" peak.[99−101] Indeed, the XANES part of the Pt L_3-edge mainly promotes core $2p_{3/2}$ electrons into empty $5d_{3/2}$, $5d_{5/2}$, and 6s valence states, so mainly probing the unoccupied density of 5d-states and partially 6s-states. The formal electronic configuration of platinum depends on its oxidation state as follows: Pt^0 ($6s^1 5d^9$), Pt^{II} ($6s^0 5d^8$), and Pt^{IV} ($6s^0 5d^6$); consequently an increase of the Pt oxidation states
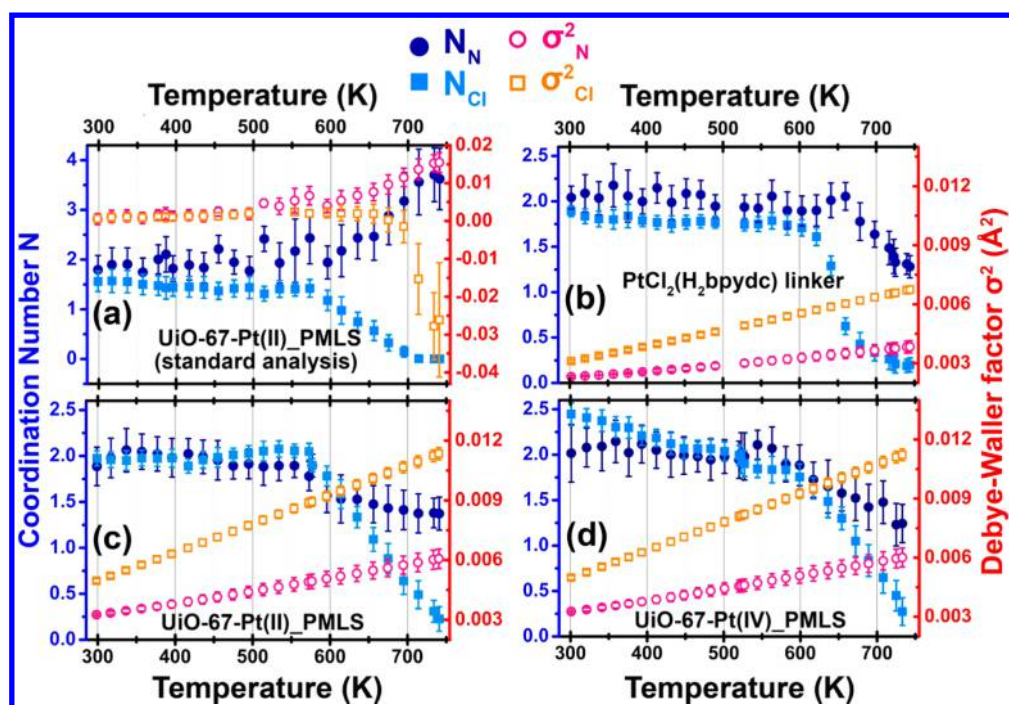
Figure 7. Part (a): standard analysis of the operando TPR-EXAFS series of spectra collected on UiO-67-Pt(II)_PMLS. Each EXAFS spectrum has been analyzed as single datum, independently from the other spectra. In the (300−600) K range, although relatively high error bars and some nonphysical oscillations, reported values are meaningful. In the 600−750 K range reported values correspond to good mathematical fits of the experimental data, that has however no physical meaning. Parts (b)-(d): final refinement of the operando TPR-EXAFS experiments on PtCl₂(H₂bpydc) linker and on UiO-67-Pt(II)_PMLS, UiO-67-Pt(II)_OPS, and UiO-67-Pt(IV)_PMLS, respectively. Data referring to the Pt−N and Pt−Cl bonds are reported as blue and cyan full-symbols and refer to the left ordinate axes. Corresponding Debye−Waller factors are reported as pink and orange open symbols and refer to the right ordinate axes. The latter were refined with a parametric approach using the Einstein model, see eq 1. The Einstein temperatures Θ_E obtained for both Pt−N and Pt−Cl bonds from this study are reported in Table 2. All experiments were performed adopting a temperature gradient of 3 K min⁻¹. A selection of the experimental data used in these analyses is reported in Figure 6.

results in a higher density of unoccupied 5d states (and 6s) that is directly measured by an increase in the intensity of Pt L₃-edge.[99−101] The XANES spectra reported in Figure 6a for UiO-67-Pt(II)_PMLS MOF clearly show a small, but meaningful decrease of the white-line intensity starting from 580 K testifying that the loss of Cl⁻ ligands (see Figure 7c) is accompanied by a decrease of the density of the unoccupied 5d states, reflecting a formal progressive reduction of Pt^{II} toward isolated Pt^0 atoms linked to the framework of the functionalized UiO-67 MOF via Pt−N bonds in bpydcPt^0 complexes.

As Pt-hydride complexes are well-known in the literature,[102−104] the observed EXAFS and XANES evidence could also be interpreted in terms of the formation of a platinum hydride complex, according to the successive two path reaction: (i) bpydcPtCl₂ + H₂ → bpydcPtClH + HCl and (ii) bpydcPtClH + H₂ → bpydcPtH₂ + HCl. Indeed the eventual presence of two hydrogen atoms in the first coordination shell of platinum will be almost undetectable from Pt L₃-edge EXAFS owing to the negligible scattering amplitude of H atoms (only in very limited and specific cases the presence of H has been detected by EXAFS[105,106]). On a simple stoichiometric point of view, hydrogen species substituting Cl⁻ species in a bpydcPt are formally expected to be anionic H⁻ species, so that platinum in the hydride bpydcPtH₂ complex is formally a Pt^{II} species. However, as platinum and hydrogen have a very similar electron affinity, an important fraction of the charge of the H⁻ anion is transferred into the 5d electrons of platinum, with a consequent relative decrease of the density of unoccupied Pt 5d states moving from bpydcPtCl₂ to bpydcPtH₂ complex. This

means that the qualitative decrease of the Pt L₃-edge white-line peak observed in the TPR-XANES experiment (Figure 6a) is compatible also with the formation of Pt hydride complexes. This hypothesis will however be ruled out by IR spectroscopy, as described in the next section.

3.2.3. IR Spectroscopy of Adsorbed CO on H₂-Activated Pt-Functionalized UiO-67 MOFs. Contrarily to the difficulties intrinsically related to X-ray based techniques, the determination of the possible formation of Pt-hydride complexes can be easily assessed IR spectroscopy, as Pt−H species result in Pt−H stretching modes absorbing in the 2240−2040 cm⁻¹ range.[107,108] We collected IR spectra on UiO-67-Pt(II)_PSF and on UiO-67-Pt(IV)_PSF samples before and after H₂-reduction. As, in both cases, no absorption band appeared in the 2240−2040 cm⁻¹ range, we exclude the formation bpydcPtClH and bpydcPtH₂ hydride complexes on Pt-functionalized UiO-67 samples upon H₂-reduction.

To further investigate the final coordination and oxidation state reached by Pt after the H₂-activation procedure and the consequent removal of the Cl ligands, we performed FTIR spectroscopy of adsorbed CO. Indeed, this technique has been widely employed to study the local environment and oxidation state of reactive surface species.[109−114] In particular, FTIR shed light on Pt nanoparticles[115] on isolated Pt charge-balancing sites in zeolites[116−119] and on metallorganic complexes.[120−123] Unperturbed CO molecules in the gas phase are characterized by a C−O stretching frequency $\tilde{\nu}_0(CO)$ = 2143 cm⁻¹, that is modified once adsorbed on a surface site M due to the nature of the M−CO interaction. Three different effects contribute in

defining the $\tilde{\nu}(CO)$ value of the adsorbed molecule: (i) electrostatic effect due to the charge of M (proportional to the ratio between the charge/radius of M);[51,126−128] (ii) σ-donation from CO σ molecular orbital;[51] and (iii) π-back-donation from M d-orbitals into CO antibonding π molecular orbital.[51] Effects (i) and (ii) result in a strengthening of the C−O bond with a consequent blue-shift of the $\tilde{\nu}(CO)$, while effect (iii) weakens the molecular bond, with a consequent $\tilde{\nu}(CO)$ red-shift. On these bases, moving from Pt^{n+} to Pt^0, a progressive decrease of $\tilde{\nu}(CO)$ of the corresponding carbonyls is observed, because of the concomitant decrease of the electrostatic effect and of the increase of the π-back-donation due to an increased d-density of states at the Pt site.

Figure 8 shows the IR spectra, in the C−O stretching region, collected during CO adsorption experiment performed on a
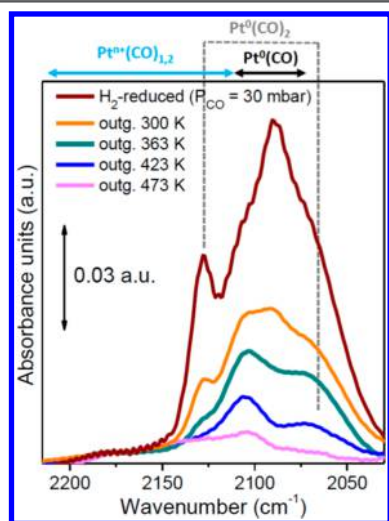
Figure 8. Room temperature FTIR spectra of CO adsorbed on the H$_2$-reduced UiO-67-Pt(IV)_PSF MOF activated at 650 K and progressive CO outgassing at increasing temperatures. All spectra have been background subtracted, using the spectrum collected before CO dosage as background. The top part of the figure reports a simplified scheme of the spectral regions where the C−O stretching frequency of linear Pt-carbonyls is expected on the basis of the Pt oxidation state and of the carbonyl stoichiometry.

UiO-67-Pt(IV)_PSF MOF sample after in situ H$_2$-reduction at 650 K. At the lowest CO coverage we observe a single broad, red-shifted, band centered around 2105 cm^{-1}, $\Delta\tilde{\nu}(CO) = -38$ cm^{-1}, typical of linear monocarbonyls on Pt^0 or Pt^I sites.[116−118] Upon increasing the CO coverage, this band further develops showing an even greater heterogeneity, and it is successively accompanied by a doublet at 2126 and 2090 cm^{-1}, that is interpreted as Pt^0(CO)$_2$ dicarbonyl adducts. The absence of CO bands in the 1900−1750 cm^{-1} region, typical of bridged CO on Pt metal,[35,115] discards the presence of Pt nanoparticles, in agreement with the EXAFS results.

Ideally, the presence of bpydcPt^0 complexes grafted in the UiO-67 framework is expected to result in very well-defined bpydcPt^{0}CO adducts (characterized by a narrow IR band), that should first increase in intensity upon increasing CO coverage and then decrease due to the successive formation of bpydcPt^0(CO)$_2$ adducts (characterized by two narrow IR bands). In the CO-coverage dependent IR spectra two isosbestic points should monitor the M(CO) → M(CO)$_2$ transformation.[51,129−132] The IR spectra reported in Figure 8 show a less defined situation where the heterogeneity of the

adsorbing site is evident. The heterogeneity monitored by IR is actually in agreement with the EXAFS results (showing average coordination numbers $N_N < 2$ and $N_{Cl} \neq 0$, see Figure 7) suggesting that, at the end of the H$_2$-reduction treatment, together with bpydcPt^0, also bpydcPt^{I}Cl complexes are expected, together with situations where Pt atoms are linked to the bpydc via a single Pt−N bond. Summarizing, IR spectroscopy is compatible with a variety of Pt−carbonyl complexes such as bpydcPt^0(CO), bpydcPt^{I}Cl(CO), bpydcPt^0(CO)$_2$, and mono- and dicarbonyl complexes on platinum atoms linked to framework bpydc via a single Pt−N bond. In all cases the spectroscopic region where platinum−carbonyls were observed by IR spectroscopy is in agreement with the XANES results which suggest a progressive reduction of Pt toward Pt^0 during the H$_2$-TPR experiments, monitored by an increased population of Pt 5d states.

3.3. Reactivity toward H$_2$tdt and Br$_2$. In order to further check the reactivity of square planar Pt(II) species inserted in the UiO-67 framework, we have used EXAFS spectroscopy to check the modification of the local environment of platinum after interaction with H$_2$tdt and Br$_2$ molecules from the liquid phase, see the experimental section (2.1.2). Figure 9a reports
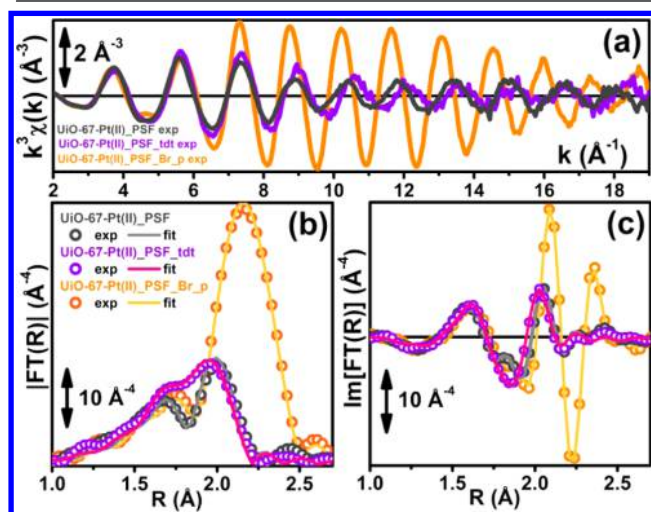

Figure 9. Part (a): experimental Pt L$_3$-edge $k^3\chi(k)$ spectra of UiO-67-Pt(II)_PSF before (black line) and after interaction with H$_2$tdt (violet line) and Br$_2$ in 2-propanol (orange line). Part (b): modulus of the k^3-weighted, phase uncorrected FT of the experimental EXAFS spectra reported in part (a), open symbols, same color code as in part (a). Also reported, as solid lines of similar color, are the corresponding best fits (see Table 5 for the quantitative results). Part (c): as part (b) for the imaginary parts of the k^3-weighted, phase uncorrected FT.

the $k^3\chi(k)$ spectra of UiO-67-Pt(II)_PSF MOF before (black line) and after interaction with H$_2$tdt and Br$_2$ in 2-propanol, violet and orange lines, respectively. The spectrum obtained on UiO-67-Pt(II)_PSF MOF after interaction with Br$_2$ in octane (not reported) is very similar to that obtained after interaction with Br$_2$ in the 2-propanol solution. Remarkable is the fact that up to 6 Å^{-1} the three spectra are very similar. This is the spectral region where the N ligands provide their major contribution to the overall EXAFS spectrum, while at higher k values the contributions from the heavier Cl, S, and Br ligands dominate. The relevant changes present in the EXAFS spectrum in the (6−18) Å^{-1} range reflect the fact that the interaction with H$_2$tdt (Br$_2$) resulted in the Cl to S (Br) ligand exchange. Impressive is the increase in the intensity of the Pt

Table 5. Summary of the Fits Performed on the Static EXAFS Spectra Collected at RT on UiO-67-Pt(II)_PSF MOF after Interaction with H$_2$tdt and Br$_2$ in Solution of 2-Propanol or Octane, First, Second, and Third Rows, Respectively[a]

sample	shell	N	σ^2 (Å^2)	R (Å)	E$_0$ (eV)	S$_0^2$	R-factor
UiO-67-Pt(II)_PSF_tdt	Pt−N	2	0.004 ± 0.001	2.04 ± 0.01	0 ± 2	0.92	0.016
	Pt−S	1.9 ± 0.2	0.003 ± 0.001	2.281 ± 0.007			
UiO-67-Pt(II)_PSF_Br_o	Pt−N	2	0.003 ± 0.001	2.05 ± 0.01	−3 ± 1	0.92	0.009
(octane)	Pt−Br	3.5 ± 0.3	0.003 ± 0.001	2.445 ± 0.004			
UiO-67-Pt(II)_PSF_Br_p	Pt−N	2	0.003 ± 0.001	2.048 ± 0.008	−1 ± 1	0.92	0.005
(2-propanol)	Pt−Br	3.6 ± 0.3	0.003 ± 0.001	2.446 ± 0.004			

[a]$\Delta k = (3.2-18.5)$ Å^{-1}; $\Delta R = (1.10-2.65)$ Å. See section 2.1.2 for the details on the ligand exchange procedure. Underlined numbers refer to not optimized parameters. The graphical quality of the fit can be appreciated in Figure 9.
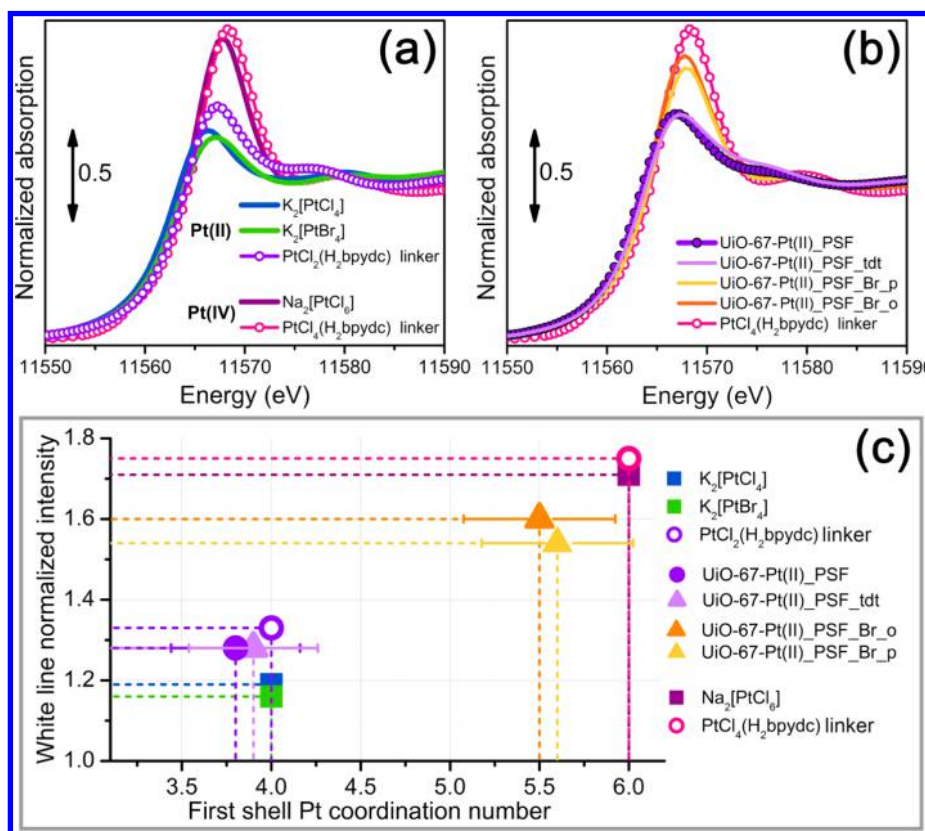
Figure 10. Part (a): Pt L$_3$-edge XANES spectra of model compounds exhibiting well-defined coordination and oxidation states. Part (b): as part (a) for a selection of Pt-functionalized MOFs discussed in this work; the spectrum of PtCl$_4$(H$_2$bpydc) linker is also reported for comparison with a well-defined Pt(IV) system. Part (c): correlation between the overall Pt first shell coordination number ($N_{tot} = N_N + N_X$, being X = Cl, S, or Br) and the white-line intensity in the normalized Pt L$_3$-edge XANES spectra. For model compounds, where the N_{tot} results from diffraction studies,[133−135] no incertitude bars have been reported, while for samples where N_{tot} has been obtained from the refinements of the EXAFS data summarized in Table 3, Table 4, and Table 5, error bars have been reported in quadrature: $\Delta N_{tot} = [(\Delta N_N)^2 + (\Delta N_X)^2]^{1/2}$.

L$_3$-edge EXAFS oscillations upon Br insertion in the first coordination shell of Pt. The changes induced by the replacement of the Cl with the almost isoelectronic S ligand are less pronounced; however, a change of phase is clearly observed for $k > 9$ Å^{-1}. Parts (b) and (c) of Figure 9 report, using the same color code, the modulus and the imaginary part of the k^3-weighted FT of EXAFS spectra reported in part (a). As usual, the imaginary part (Figure 9c) is more informative than the modulus (Figure 9b). Indeed, the imaginary part shows that, in the 1.0−1.7 Å region, the three spectra are characterized by almost the same signal, mainly due to the two N ligands of the bpydc linker. This observation allowed us to fix the coordination number of the N atoms to the value optimized in the fit of the UiO-67-Pt(II)_PSF spectrum, i.e. $N_N = 2.0$, see Table 3. The substitution of Cl with S results in a small shift of

the imaginary part in the 1.7−2.2 Å region, while the insertion of Br shifts the signal at higher R values and increases remarkably its intensity.

On these bases, the EXAFS fits can be performed by fixing S_0^2 to 0.92 (as discussed above) and N_N to 2.0. Fixing these two parameters significantly contributes to the reduction of the correlation among the remaining optimized parameters and to the overall stability of the fits. The results are summarized in Table 5, while the fit quality can be visually appreciated in R-space in Figure 9b,c, where the best fit curves are superimposed with the experimental spectra, reported as open circles, using full lines with similar color codes.

The results of the fit on UiO-67-Pt(II)_PSF_tdt clearly show that a complete substitution of the two Cl ligands with two S atoms of the chelating H$_2$tdt molecule has been obtained. On

both UiO-67-Pt(II)_PSF_Br_o and UiO-67-Pt(II)_PSF_Br_p samples, the replacement of two Cl$^-$ by almost four Br$^-$ ligands in the first coordination shell of platinum suggests that Br$_2$ is able to oxidize Pt(II) into Pt(IV). Further confirmation of this EXAFS evidence comes from the study of the XANES part of the X-ray absorption spectra. Indeed, as discussed above, the intensity of the white-line of Pt L$_3$-edge XANES spectra directly reflect the density of unoccupied 5d states of Pt and thus can be used to follow changes in the oxidation state of the metal center, see Figure 6a and Figure 10a reporting some Pt L$_3$-edge XANES spectra of model compounds. The XANES spectra of UiO-67-Pt(II)_PSF and UiO-67-Pt(II)_PSF_tdt samples are characterized by a white-line of very similar intensity (Figure 10b), testifying that the oxidation state of Pt is not affected by the Cl to S ligand exchange. Conversely, the important increase observed after interaction with Br$_2$ reflects a significant decrease in the 5d density of occupied states, compatible with a formal oxidation state close to Pt^{IV}, in agreement with the coordination of almost four Br atoms. Part (c) of Figure 10 reports the qualitative correlation observed plotting the measured white-line intensity of the normalized XANES spectra versus the overall first shell coordination number determined in the EXAFS data analysis.

Summarizing, EXAFS experiments (Table 5) revealed that interaction with H$_2$tdt and Br$_2$ does not affect the Pt−N bonds anchoring platinum to the MOF framework via the bpydc linker and that Cl ligands are fully substituted by S ligands of the H$_2$tdt chelating complex or by Br atoms. In the latter case, a coordination number N_{Br} close to 4 indicates that the interaction with Br$_2$ (in both 2-propanol or octane solutions) results in the oxidation of the platinum centers from Pt(II) to Pt(IV). This evidence is also supported by the increase of the white-line in the XANES part of the Pt L$_3$-edge X-ray absorption spectra (Figure 10).

4. CONCLUSIONS

In this work we present three methods (see Figure 2a-c) of the synthesis of UiO-67 functionalized with bpydcPt^{II}Cl$_2$ and bpydcPt^{IV}Cl$_4$ coordination complexes acting as linkers in the MOF framework: (i) one-pot synthesis (OPS) where ZrCl$_4$ and PtCl$_x$ (x = 2 or 4) precursors salts react with biphenyl and bipyridine linkers; (ii) premade linker synthesis (PMLS), where previously prepared PtCl$_x$(H$_2$bpydc) linker reacts with biphenyl linkers and ZrCl$_4$; and (iii) postsynthesis functionalization (PSF), where premade UiO-67-bpy MOF is suspended in a solution of precursor PtCl$_x$ salt. With the only exception of the UiO-67-Pt(II)-OPS, that crystallize together with a fraction of about 40% of amorphous (nonporous) phase, the remaining syntheses resulted in high crystalline materials with porosity close to the target ideal structure. XRPD and Pt L$_3$-EXAFS studies prove that the three synthesis methods are equivalent and comply with the target structure (Figure 2d) on both long-range (ordered MOF framework) and short-range (local environment of Pt sites) scales. The last point has also been supported by Pt L$_3$ valence-to-core RIXS on UiO-67-Pt(II)_PMLS sample. For UiO-67-Pt(II)-OPS this holds for the 60% of the crystalline fraction and means that Pt(II) does not enter in the amorphous phase in an appreciable amount.

With respect to other Pt-MOFs previously synthesized by our group,[55,56] UiO-67-Pt(II) and UiO-67-Pt(IV) MOFs presented in this work show a high accessibility and reactivity to molecules of small- (H$_2$), medium- (Br$_2$), and large-size (thiol), as schematized in Figure 11. H$_2$-TPR treatments have
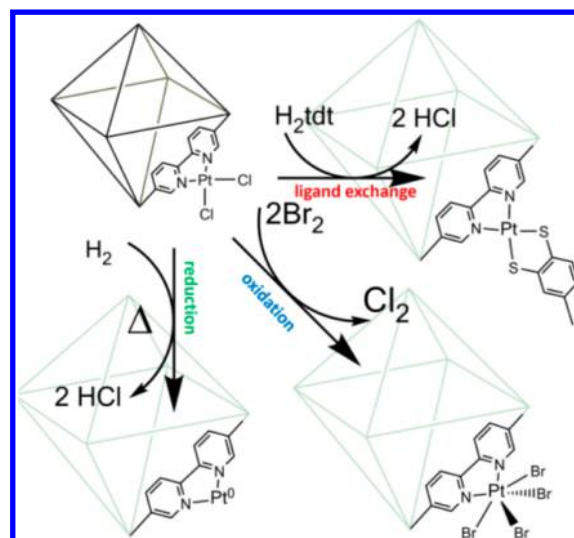
Figure 11. Schematic representation of the reactivity of Pt^{II} species in functionalized UiO-67-Pt MOFs that has been highlighted in the EXAFS and XANES study reported in this work. The sketched square bipyramid represents the octahedral large cavity of UiO-67, measuring about 16 Å in diagonal.[21,22]

been followed under *operando* conditions by EXAFS, showing that Cl ligands can be selectively removed as HCl molecules in the 600−700 K temperature range, resulting in bpydcPt^0 complexes linked to the MOF framework (reduction path in Figure 11). This result has been obtained after sophisticated parametric refinement, where all EXAFS spectra collected in the 300−750 K range have been refined together adopting the Einstein model for the Pt−N and Pt−Cl Debye−Waller factors. IR spectroscopy testifies the high coordinative unsaturation of reduced platinum centers, able to form a variety of Pt monocarbonyl complexes and also bpydcPt^0(CO)$_2$ dicarbonyl complexes upon CO adsorption. The large pore size of UiO-67 allows for ligand exchange between 2 Cl$^-$ and even bulky ligands such as toluene-3,4-dithiol (ligand exchange path in Figure 11). Framework bpydcPt^{II}Cl$_2$ complexes can also be oxidized at room temperature to bpydcPt^{IV}Br$_4$ through oxidative addition of liquid Br$_2$ (oxidation path in Figure 11). XANES spectroscopy was used to monitor the changes in the Pt oxidation state along the observed reactions, while EXAFS monitored the ligand exchange in the fist coordination shell of Pt. Platinum bipyridine functionalized UiO-67 displays the same exceptional stability as the parent UiO-66 and UiO-67 materials,[21,22,44,136] as testified on both long and local range by in situ XRPD and Pt L$_3$-edge EXAFS data collections.

■ ASSOCIATED CONTENT

ⓢ Supporting Information

Additional details on the linkers (H$_2$bpydc, PtCl$_2$(H$_2$bpydc), PtCl$_4$(H$_2$bpydc) and PtBr$_4$(H$_2$bpydc)) synthesis, corresponding ^{1}H solid state NMR spectra, and results on the single crystal XRD structure refinement. Additional details on the MOF synthesis and corresponding BET measurements. Elemental analysis, SEM analysis, and *operando* TPR-EXAFS experiment on the UiO-67-Pt(II)-OPS sample. This material is available free of charge via the Internet at http://pubs.acs.org.

■ AUTHOR INFORMATION

Corresponding Authors

*Phone: 39011-6707841. Fax: 39011-6707855. E-mail: carlo.lamberti@unito.it (C.L.).
*Phone: 4722855457. E-mail: k.p.lillerud@kjemi.uio.no (K.-P.L.).

Notes

The authors declare no competing financial interest.

■ REFERENCES

(1) Tranchemontagne, D. J.; Mendoza-Cortes, J. L.; O'Keeffe, M.; Yaghi, O. M. *Chem. Soc. Rev.* **2009**, *38*, 1257.

(2) Llabrés i Xamena, F. X.; Abad, A.; Corma, A.; Garcia, H. *J. Catal.* **2007**, *250*, 294.

(3) Lee, J.; Farha, O. K.; Roberts, J.; Scheidt, K. A.; Nguyen, S. T.; Hupp, J. T. *Chem. Soc. Rev.* **2009**, *38*, 1450.

(4) Ma, L.; Abney, C.; Lin, W. *Chem. Soc. Rev.* **2009**, *38*, 1248.

(5) Corma, A.; García, H.; Llabrés i Xamena, F. X. *Chem. Rev.* **2010**, *110*, 4606.

(6) Ranocchiari, M.; van Bokhoven, J. A. *Phys. Chem. Chem. Phys.* **2011**, *13*, 6388.

(7) Llabrés i Xamena, F. X.; Gascón, J. *Metal Organic Frameworks as Heterogeneous Catalysts*; The Royal Society of Chemistry: Cambridge, 2013; p 1.

(8) Dinca, M.; Long, J. R. *J. Am. Chem. Soc.* **2005**, *127*, 9376.

(9) Bae, Y. S.; Farha, O. K.; Spokoyny, A. M.; Mirkin, C. A.; Hupp, J. T.; Snurr, R. Q. *Chem. Commun.* **2008**, 4135.

(10) Li, J.-R.; Luppler, R. J.; Zhou, H. C. *Chem. Soc. Rev.* **2009**, *38*, 1477.

(11) Tanaka, D.; Henke, A.; Albrecht, K.; Moeller, M.; Nakagawa, K.; Kitagawa, S.; Groll, J. *Nat. Chem.* **2010**, *2*, 410.

(12) Matsuda, R.; Tsujino, T.; Sato, H.; Kubota, Y.; Morishige, K.; Takata, M.; Kitagawa, S. *Chem. Sci.* **2010**, *1*, 315.

(13) Rodenas, T.; Luz, I.; Prieto, G.; Seoane, B.; Miro, H.; Corma, A.; Kapteijn, F.; Llabrés i Xamena, F. X.; Gascon, J. *Nat. Mater.* **2015**, *14*, 48.

(14) Wang, Z.; Cohen, S. M. *Chem. Soc. Rev.* **2009**, *38*, 1315.

(15) Deng, H. X.; Doonan, C. J.; Furukawa, H.; Ferreira, R. B.; Towne, J.; Knobler, C. B.; Wang, B.; Yaghi, O. M. *Science* **2010**, *327*, 846.

(16) Chen, B. L.; Xiang, S. C.; Qian, G. D. *Acc. Chem. Res.* **2010**, *43*, 1115.

(17) Kandiah, M.; Usseglio, S.; Svelle, S.; Olsbye, U.; Lillerud, K. P.; Tilset, M. *J. Mater. Chem.* **2010**, *20*, 9848.

(18) Chavan, S.; Vitillo, J. G.; Uddin, M. J.; Bonino, F.; Lamberti, C.; Groppo, E.; Lillerud, K. P.; Bordiga, S. *Chem. Mater.* **2010**, *22*, 4602.

(19) Tanabe, K. K.; Cohen, S. M. *Chem. Soc. Rev.* **2011**, *40*, 498.

(20) Cohen, S. M. *Chem. Rev.* **2012**, *112*, 970.

(21) Cavka, J. H.; Jakobsen, S.; Olsbye, U.; Guillou, N.; Lamberti, C.; Bordiga, S.; Lillerud, K. P. *J. Am. Chem. Soc.* **2008**, *130*, 13850.

(22) Chavan, S.; Vitillo, J. G.; Gianolio, D.; Zavorotynska, O.; Civalleri, B.; Jakobsen, S.; Nilsen, M. H.; Valenzano, L.; Lamberti, C.; Lillerud, K. P.; Bordiga, S. *Phys. Chem. Chem. Phys.* **2012**, *14*, 1614.

(23) Wang, C.; Xie, Z. G.; deKrafft, K. E.; Lin, W. L. *J. Am. Chem. Soc.* **2011**, *133*, 13445.

(24) Fei, H. H.; Cohen, S. M. *Chem. Commun.* **2014**, *50*, 4810.

(25) Crabtree, R. H. *Chem. Rev.* **1995**, *95*, 987.

(26) Arakawa, H.; Aresta, M.; Armor, J. N.; Barteau, M. A.; Beckman, E. J.; Bell, A. T.; Bercaw, J. E.; Creutz, C.; Dinjus, E.; Dixon, D. A.; Domen, K.; DuBois, D. L.; Eckert, J.; Fujita, E.; Gibson, D. H.; Goddard, W. A.; Goodman, D. W.; Keller, J.; Kubas, G. J.; Kung, H. H.; Lyons, J. E.; Manzer, L. E.; Marks, T. J.; Morokuma, K.; Nicholas, K. M.; Periana, R.; Que, L.; Rostrup-Nielson, J.; Sachtler, W. M. H.; Schmidt, L. D.; Sen, A.; Somorjai, G. A.; Stair, P. C.; Stults, B. R.; Tumas, W. *Chem. Rev.* **2001**, *101*, 953.

(27) Shilov, A. E.; Shul'pin, G. B. *Chem. Rev.* **1997**, *97*, 2879.

(28) Labinger, J. A.; Bercaw, J. E. *Nature* **2002**, *417*, 507.

(29) Lersch, M.; Tilset, M. *Chem. Rev.* **2005**, *105*, 2471.

(30) Wolf, D. *Angew. Chem., Int. Ed.* **1998**, *37*, 3351.

(31) Periana, R. A.; Taube, D. J.; Gamble, S.; Taube, H.; Satoh, T.; Fujii, H. *Science* **1998**, *280*, 560.

(32) Palkovits, R.; Antonietti, M.; Kuhn, P.; Thomas, A.; Schüth, F. *Angew. Chem., Int. Ed.* **2009**, *48*, 6909.

(33) Palkovits, R.; von Malotki, C.; Baumgarten, M.; Mullen, K.; Baltes, C.; Antonietti, M.; Kuhn, P.; Weber, J.; Thomas, A.; Schüth, F. *ChemSusChem* **2010**, *3*, 277.

(34) Soorholtz, M.; White, R. J.; Zimmermann, T.; Titirici, M. M.; Antonietti, M.; Palkovits, R.; Schüth, F. *Chem. Commun.* **2013**, *49*, 240.

(35) Bordiga, S.; Bonino, F.; Lillerud, K. P.; Lamberti, C. *Chem. Soc. Rev.* **2010**, *39*, 4885.

(36) Bordiga, S.; Groppo, E.; Agostini, G.; van Bokhoven, J. A.; Lamberti, C. *Chem. Rev.* **2013**, *113*, 1736.

(37) Borfecchia, E.; Gianolio, D.; Agostini, G.; Bordiga, S.; Lamberti, C. Characterization of MOFs. 2. Long and Local Range Order Structural Determination of MOFs by Combining EXAFS and Diffraction Techniques. In *Metal Organic Frameworks as Heterogeneous Catalysts*; Llabrés i Xamena, F. X., Gascón, J., Eds.; The Royal Society of Chemistry: Cambridge, 2013; pp 143.

(38) Garino, C.; Borfecchia, E.; Gobetto, R.; van Bokhoven, J. A.; Lamberti, C. *Coord. Chem. Rev.* **2014**, *277−278*, 130.

(39) Schaate, A.; Roy, P.; Godt, A.; Lippke, J.; Waltz, F.; Wiebcke, M.; Behrens, P. *Chem.—Eur. J.* **2011**, *17*, 6643.

(40) Walton, K. S.; Snurr, R. Q. *J. Am. Chem. Soc.* **2007**, *129*, 8552.

(41) Shearer, G. C.; Chavan, S.; Ethiraj, J.; Vitillo, J. G.; Svelle, S.; Olsbye, U.; Lamberti, C.; Bordiga, S.; Lillerud, K. P. *Chem. Mater.* **2014**, *26*, 4068.

(42) Wu, H.; Chua, Y. S.; Krungleviciute, V.; Tyagi, M.; Chen, P.; Yildirim, T.; Zhou, W. *J. Am. Chem. Soc.* **2013**, *135*, 10525.

(43) Vermoortele, F.; Bueken, B.; Le Bars, G.; Van de Voorde, B.; Vandichel, M.; Houthoofd, K.; Vimont, A.; Daturi, M.; Waroquier, M.; Van Speybroeck, V.; Kirschhock, C.; De Vos, D. E. *J. Am. Chem. Soc.* **2013**, *135*, 11465.

(44) Jakobsen, S.; Gianolio, D.; Wragg, D. S.; Nilsen, M. H.; Emerich, H.; Bordiga, S.; Lamberti, C.; Olsbye, U.; Tilset, M.; Lillerud, K. P. *Phys. Rev. B* **2012**, *86*, No. 125429.

(45) Connolly, M. L. *Science* **1983**, *221*, 709.

(46) Grehk, T. M.; Nilsson, P. O. *Nucl. Instrum. Methods Phys. Res., Sect. A* **2001**, *467*, 635.

(47) Carlson, S.; Clausen, M.; Gridneva, L.; Sommarin, B.; Svensson, C. *J. Synchrotron Radiat.* **2006**, *13*, 359.

(48) Lamberti, C.; Prestipino, C.; Bordiga, S.; Berlier, G.; Spoto, G.; Zecchina, A.; Laloni, A.; La Manna, F.; D'Anca, F.; Felici, R.; D'Acapito, F.; Roy, P. *Nucl. Instrum. Methods Phys. Res., Sect. B* **2003**, *200*, 196.

(49) Lamberti, C.; Prestipino, C.; Bonino, F.; Capello, L.; Bordiga, S.; Spoto, G.; Zecchina, A.; Moreno, S. D.; Cremaschi, B.; Garilli, M.; Marsella, A.; Carmello, D.; Vidotto, S.; Leofanti, G. *Angew. Chem., Int. Ed.* **2002**, *41*, 2341.

(50) Lamberti, C.; Bordiga, S.; Bonino, F.; Prestipino, C.; Berlier, G.; Capello, L.; D'Acapito, F.; Llabrés i Xamena, F. X.; Zecchina, A. *Phys. Chem. Chem. Phys.* **2003**, *5*, 4502.

(51) Bolis, V.; Barbaglia, A.; Bordiga, S.; Lamberti, C.; Zecchina, A. *J. Phys. Chem. B* **2004**, *108*, 9970.

(52) Groppo, E.; Prestipino, C.; Cesano, F.; Bonino, F.; Bordiga, S.; Lamberti, C.; Thune, P. C.; Niemantsverdriet, J. W.; Zecchina, A. *J. Catal.* **2005**, *230*, 98.

(53) Prestipino, C.; Solari, P. L.; Lamberti, C. *J. Phys. Chem. B* **2005**, *109*, 13132.

(54) Prestipino, C.; Regli, L.; Vitillo, J. G.; Bonino, F.; Damin, A.; Lamberti, C.; Zecchina, A.; Solari, P. L.; Kongshaug, K. O.; Bordiga, S. *Chem. Mater.* **2006**, *18*, 1337.

(55) Szeto, K. C.; Lillerud, K. P.; Tilset, M.; Bjorgen, M.; Prestipino, C.; Zecchina, A.; Lamberti, C.; Bordiga, S. *J. Phys. Chem. B* **2006**, *110*, 21509.

(56) Szeto, K. C.; Prestipino, C.; Lamberti, C.; Zecchina, A.; Bordiga, S.; Bjorgen, M.; Tilset, M.; Lillerud, K. P. *Chem. Mater.* **2007**, *19*, 211.

(57) Hafizovic, J.; Bjorgen, M.; Olsbye, U.; Dietzel, P. D. C.; Bordiga, S.; Prestipino, C.; Lamberti, C.; Lillerud, K. P. *J. Am. Chem. Soc.* **2007**, *129*, 3612.

(58) Agostini, G.; Usseglio, S.; Groppo, E.; Uddin, M. J.; Prestipino, C.; Bordiga, S.; Zecchina, A.; Solari, P. L.; Lamberti, C. *Chem. Mater.* **2009**, *21*, 1343.

(59) Agostini, G.; Pellegrini, R.; Leofanti, G.; Bertinetti, L.; Bertarione, S.; Groppo, E.; Zecchina, A.; Lamberti, C. *J. Phys. Chem. C* **2009**, *113*, 10485.

(60) Muddada, N. B.; Olsbye, U.; Caccialupi, L.; Cavani, F.; Leofanti, G.; Gianolio, D.; Bordiga, S.; Lamberti, C. *Phys. Chem. Chem. Phys.* **2010**, *12*, 5605.

(61) Muddada, N. B.; Olsbye, U.; Leofanti, G.; Gianolio, D.; Bonino, F.; Bordiga, S.; Fuglerud, T.; Vidotto, S.; Marsella, A.; Lamberti, C. *Dalton Trans.* **2010**, *39*, 8437.

(62) Gianolio, D.; Muddada, N. B.; Olsbye, U.; Lamberti, C. *Nucl. Instrum. Methods Phys. Res., Sect. B* **2012**, *284*, 53.

(63) Ravel, B.; Newville, M. *J. Synchrotron Radiat.* **2005**, *12*, 537.

(64) Lamberti, C.; Bordiga, S.; Arduino, D.; Zecchina, A.; Geobaldo, F.; Spano, G.; Genoni, F.; Petrini, G.; Carati, A.; Villain, F.; Vlaic, G. *J. Phys. Chem. B* **1998**, *102*, 6382.

(65) Ankudinov, A. L.; Ravel, B.; Rehr, J. J.; Conradson, S. D. *Phys. Rev. B* **1998**, *58*, 7565.

(66) Hafizovic, J.; Olsbye, U.; Lillerud, K. P. *Acta Crystallogr., Sect. E: Struct. Rep. Online* **2006**, *E62*, M414.

(67) Newville, M. *J. Synchrotron Radiat.* **2001**, *8*, 322.

(68) Beni, G.; Platzman, P. M. *Phys. Rev. B* **1976**, *14*, 1514.

(69) Sevillano, E.; Meuth, H.; Rehr, J. J. *Phys. Rev. B* **1979**, *20*, 4908.

(70) Poiarkova, A. V.; Rehr, J. J. *Phys. Rev. B* **1999**, *59*, 948.

(71) Dimakis, N.; Bunker, G. *Phys. Rev. B* **1998**, *58*, 2467.

(72) Rehr, J. J.; Albers, R. C. *Rev. Mod. Phys.* **2000**, *72*, 621.

(73) Dimakis, N.; Bunker, G. *Phys. Rev. B* **2002**, *65*, No. 201103.

(74) Einstein, A. *Ann. Phys.* **1907**, *22*, 180.

(75) Menushenkov, A. P.; Benazeth, S.; Purans, J.; Ignatov, A. Y.; Klementev, K. V. *Physica C* **1997**, *277*, 257.

(76) VanHung, N.; Rehr, J. J. *Phys. Rev. B* **1997**, *56*, 43.

(77) Dalba, G.; Fornasini, P.; Grisenti, R.; Purans, J. *Phys. Rev. Lett.* **1999**, *82*, 4240.

(78) Dubiel, M.; Brunsch, S.; Seifert, W.; Hofmeister, H.; Tan, G. L. *Eur. Phys. J. D* **2001**, *16*, 229.

(79) Ghigna, P.; Carollo, A.; Flor, G.; Malavasi, L.; Peruga, G. S. *J. Phys. Chem. B* **2005**, *109*, 4365.

(80) Vaccari, M.; Fornasini, P. *J. Synchrotron Radiat.* **2006**, *13*, 321.

(81) Araujo, L. L.; Kluth, P.; Azevedo, G. D. M.; Ridgway, M. C. *Phys. Rev. B* **2006**, *74*, No. 184102.

(82) Sanson, A. *J. Synchrotron Radiat.* **2008**, *15*, 514.

(83) Schnohr, C. S.; Kluth, P.; Araujo, L. L.; Sprouster, D. J.; Byrne, A. P.; Foran, G. J.; Ridgway, M. C. *Phys. Rev. B* **2009**, *79*, No. 195203.

(84) Sprouster, D. J.; Giulian, R.; Araujo, L. L.; Kluth, P.; Johannessen, B.; Cookson, D. J.; Foran, G. J.; Ridgway, M. C. *J. Appl. Phys.* **2010**, *107*, No. 014313.

(85) Bunker, G. *Introduction to XAFS A Practical Guide to X-ray Absorption Fine Structure Spectroscopy*; Cambridge University Press: Cambridge, 2010.

(86) Agostini, A.; Grisenti, R.; Lamberti, C.; Piovano, A.; Fornasini, P. *J. Phys.: Conf. Ser.* **2013**, *430*, No. 012031.

(87) Stinton, G. W.; Evans, J. S. O. *J. Appl. Crystallogr.* **2007**, *40*, 87.

(88) Agostini, G.; Lamberti, C.; Palin, L.; Milanesio, M.; Danilina, N.; Xu, B.; Janousch, M.; van Bokhoven, J. A. *J. Am. Chem. Soc.* **2010**, *132*, 667.

(89) Glatzel, P.; Bergmann, U. *Coord. Chem. Rev.* **2005**, *249*, 65.

(90) Singh, J.; Lamberti, C.; van Bokhoven, J. A. *Chem. Soc. Rev.* **2010**, *39*, 4754.

(91) Mino, L.; Agostini, A.; Borfecchia, E.; Gianolio, D.; Piovano, A.; Lamberti, C. *J. Phys. D: Appl. Phys.* **2013**, *46*, No. 423001.

(92) Glatzel, P.; Weng, T.-C.; Kvashnina, K.; Swarbrick, J.; Sikora, M.; Gallo, E.; Smolentsev, N.; Mori, R. A. *J. Electron Spectrosc. Relat. Phenom.* **2013**, *188*, 17.

(93) S_0^2 is the so-called passive electron reduction factor, that multiplies the whole amplitude of the EXAFS signal.

(94) Kas, J. J.; Sorini, A. P.; Prange, M. P.; Cambell, L. W.; Soininen, J. A.; Rehr, J. J. *Phys. Rev. B* **2007**, *76*, No. 195116.

(95) Garino, C.; Gallo, E.; Smolentsev, N.; Glatzel, P.; Gobetto, R.; Lamberti, C.; Sadlerd, P. J.; Salassa, L. *Phys. Chem. Chem. Phys.* **2012**, *14*, 15278.

(96) Lomachenko, K. A.; Garino, C.; Gallo, E.; Gianolio, D.; Gobetto, R.; Glatzel, P.; Smolentsev, N.; Smolentsev, G.; Soldatov, A. V.; Lamberti, C.; Salassa, L. *Phys. Chem. Chem. Phys.* **2013**, *15*, 16152.

(97) Mino, L.; Borfecchia, E.; Groppo, C.; Castelli, D.; Martinez-Criado, G.; Spiess, R.; Lamberti, C. *Catal. Today* **2014**, *229*, 72.

(98) Le Toquin, R.; Paulus, W.; Cousson, A.; Prestipino, C.; Lamberti, C. *J. Am. Chem. Soc.* **2006**, *128*, 13161.

(99) Hall, M. D.; Foran, G. J.; Zhang, M.; Beale, P. J.; Hambley, T. W. *J. Am. Chem. Soc.* **2003**, *125*, 7524.

(100) Yoshida, H.; Nonoyama, S.; Yazawa, Y.; Hattori, T. *Phys. Scr.* **2005**, *T115*, 813.

(101) Beck, I. E.; Kriventsov, V. V.; Ivanov, D. P.; Zaikovsky, V. I.; Bukhtiyarov, V. I. *Nucl. Instrum. Methods Phys. Res., Sect. A* **2009**, *603*, 108.

(102) Arnold, D. P.; Bennett, M. A. *Inorg. Chem.* **1984**, *23*, 2117.

(103) Puddephatt, R. J. *Coord. Chem. Rev.* **2001**, *219−221*, 157.

(104) Webb, J. R.; Pierpont, A. W.; Munro-Leighton, C.; Gunnoe, T. B.; Cundari, T. R.; Boyle, P. D. *J. Am. Chem. Soc.* **2010**, *132*, 4520.

(105) D'Angelo, P.; Barone, V.; Chillemi, G.; Sanna, N.; Meyer-Klaucke, W.; Pavel, N. V. *J. Am. Chem. Soc.* **2002**, *124*, 1958.

(106) Balde, C. P.; Mijovilovich, A. E.; Koningsberger, D. C.; van der Eerden, A. M. J.; Smith, A. D.; de Jong, K. P.; Bitter, J. H. *J. Phys. Chem. C* **2007**, *111*, 11721.

(107) Basolo, F.; Pearson, R. G. *Prog. Inorg. Chem.* **1962**, *4*, 381.

(108) Tomonari, M.; Sugino, O. *Chem. Phys. Lett.* **2007**, *437*, 170.

(109) Zecchina, A.; Scarano, D.; Bordiga, S.; Spoto, G.; Lamberti, C. *Adv. Catal.* **2001**, *46*, 265.

(110) Spoto, G.; Gribov, E. N.; Ricchiardi, G.; Damin, A.; Scarano, D.; Bordiga, S.; Lamberti, C.; Zecchina, A. *Prog. Surf. Sci.* **2004**, *76*, 71.

(111) Lamberti, C.; Groppo, E.; Spoto, G.; Bordiga, S.; Zecchina, A. *Adv. Catal.* **2007**, *51*, 1.

(112) Lamberti, C.; Zecchina, A.; Groppo, E.; Bordiga, S. *Chem. Soc. Rev.* **2010**, *39*, 4951.

(113) Vimont, A.; Thibault-Starzyk, F.; Daturi, M. *Chem. Soc. Rev.* **2010**, *39*, 4928.

(114) Bonino, F.; Lamberti, C.; Chavan, S.; Vitillo, J. G.; Bordiga, S. Characterization of MOFs. 1. Combined Vibrational and Electronic Spectroscopies. In *Metal-Organic Frameworks in heterogeneous catalysis*; Llabrés i Xamena, F. X., Gascón, J., Eds.; RSC: Cambridge, 2013; pp 76.

(115) Visser, T.; Nijhuis, T. A.; van der Eerden, A. M. J.; Jenken, K.; Ji, Y. Y.; Bras, W.; Nikitenko, S.; Ikeda, Y.; Lepage, M.; Weckhuysen, B. M. *J. Phys. Chem. B* **2005**, *109*, 3822.

(116) Kubanek, P.; Schmidt, H. W.; Spliethoff, B.; Scuth, F. *Microporous Mesoporous Mater.* **2005**, *77*, 89.

(117) Chakarova, K.; Mihaylov, M.; Hadjiivanov, K. *Microporous Mesoporous Mater.* **2005**, *81*, 305.

(118) Chakarova, K.; Mihaylov, M.; Hadjiivanov, K. *Catal. Commun.* **2005**, *6*, 466.

(119) Daniel, C.; Clarte, M. O.; Teh, S. P.; Thinon, O.; Provendier, H.; Van Veen, A. C.; Beccard, B. J.; Schuurman, Y.; Mirodatos, C. *J. Catal.* **2010**, *272*, 55.

(120) Kündig, E. P.; McIntosh, D.; Moskovits, M.; Ozin, G. A. *J. Am. Chem. Soc.* **1973**, *95*, 7234.

(121) Li, G. J.; Fujimoto, T.; Fukuoka, A.; Ichikawa, M. *Catal. Lett.* **1992**, *12*, 171.

(122) Schulzekloff, G.; Lipski, R. J.; Jaeger, N. I.; Hulstede, P.; Kubelkova, L. *Catal. Lett.* **1995**, *30*, 65.

(123) Kubelkova, L.; Vylita, J.; Brabec, L.; Drozdova, L.; Bolom, T.; Novakova, J.; Schulz-Ekloff, G.; Jaeger, N. I. *J. Chem. Soc., Faraday Trans.* **1996**, *92*, 2035.

(124) Yamamoto, T.; Shido, T.; Inagaki, S.; Fukushima, Y.; Ichikawa, M. *J. Phys. Chem. B* **1998**, *102*, 3866.

(125) Fukuoka, A.; Osada, M.; Shido, T.; Inagaki, S.; Fukushima, Y.; Ichikawa, M. *Inorg. Chim. Acta* **1999**, *294*, 281.

(126) Zecchina, A.; Bordiga, S.; Lamberti, C.; Spoto, G.; Carnelli, L.; Arean, C. O. *J. Phys. Chem.* **1994**, *98*, 9577.

(127) Lamberti, C.; Bordiga, S.; Geobaldo, F.; Zecchina, A.; Arean, C. O. *J. Chem. Phys.* **1995**, *103*, 3158.

(128) Bordiga, S.; Lamberti, C.; Geobaldo, F.; Zecchina, A.; Palomino, G. T.; Arean, C. O. *Langmuir* **1995**, *11*, 527.

(129) Zecchina, A.; Bordiga, S.; Palomino, G. T.; Scarano, D.; Lamberti, C.; Salvalaggio, M. *J. Phys. Chem. B* **1999**, *103*, 3833.

(130) Palomino, G. T.; Bordiga, S.; Zecchina, A.; Marra, G. L.; Lamberti, C. *J. Phys. Chem. B* **2000**, *104*, 8641.

(131) Lamberti, C.; Palomino, G. T.; Bordiga, S.; Berlier, G.; D'Acapito, F.; Zecchina, A. *Angew. Chem., Int. Ed.* **2000**, *39*, 2138.

(132) Bolis, V.; Maggiorini, S.; Meda, L.; D'Acapito, F.; Palomino, G. T.; Bordiga, S.; Lamberti, C. *J. Chem. Phys.* **2000**, *113*, 9248.

(133) Kroening, R. F.; Rush, R. M.; Martin, D. S.; Clardy, J. C. *Inorg. Chem.* **1974**, *13*, 1366.

(134) Takazawa, H.; Ohba, S.; Saito, Y.; Sano, M. *Acta Crystallogr., Sect. B: Struct. Sci.* **1990**, *46*, 166.

(135) Miyoshi, H.; Horiuchi, K.; Sakagami, N.; Okamoto, K.; Ikeda, R. *Z. Naturforsch., A: Phys. Sci.* **1998**, *53*, 603.

(136) Valenzano, L.; Civalleri, B.; Bordiga, S.; Nilsen, M. H.; Jakobsen, S.; Lillerud, K.-P.; Lamberti, C. *Chem. Mater.* **2011**, *23*, 1700.